REFERENCES

[1] T. Matsumoto, "A chaotic attractor from Chua's circuit," *IEEE Trans. Circuits Syst.*, vol. CAS-31, pp. 1055–1058, Dec. 1984.
[2] G.-Q. Zhong and F. Ayrom, "Experimental confirmation of chaos from Chua's circuit," *Int. J. Circuit Theory Appl.*, vol. 13, pp. 93–98, Jan. 1985.
[3] L. O. Chua, M. Komuro, and T. Matsumoto, "The double scroll family," *IEEE Trans. Circuits Syst.*, vol. CAS-33, pp. 1072–1118, Nov. 1986.
[4] I. Mees and P. B. Chapman, "Homoclinic and heteroclinic orbits in the double scroll attractor," to appear in *IEEE Trans. Circuits Syst.*, vol. CAS-34, no. 9, Sept. 1987.
[5] J. Guckenheimer and P. Holmes, *Nonlinear Oscillations, Dynamical Systems, and Bifurcations of Vector Fields.* New York, NY: Springer-Verlag, 1983.
[6] L. O. Chua, C. A. Desoer, and E. S. Kuh, *Linear and Nonlinear Circuits.* New York, NY: McGraw-Hill, 1987.
[7] L. O. Chua, "Nonlinear circuits," *IEEE Trans. Circuits Syst.* (Centennial Special Issue), vol. CAS-31, pp. 69–87, Jan. 1984.
[8] ——, "Device modelling via basic nonlinear circuit elements," *IEEE Trans. Circuits Syst.*, vol. CAS-27, pp. 1014–1044, Nov. 1980.
[9] G.-Q. Zhong and F. Ayrom, "Periodicity and chaos in Chua's circuits," *IEEE Trans. Circuits Syst.*, vol. CAS-32, pp. 501–503, May 1985.
[10] T. Matsumoto, L. O. Chua, and M. Komuro, "The double scroll bifurcations," *Int. J. Circuit Theory Appl.*, vol. 14, pp. 117–146, Apr. 1986.
[11] M. E. Broucke, "One-parameter bifurcation diagram for Chua's circuit," *IEEE Trans. Circuits Syst.*, vol. CAS-34, pp. 208–209, Feb. 1987.
[12] L. Yang and Y. Liao, "Self-similar bifurcation structures from Chua's circuit," *Int. J. Circuit Theory Appl.*, 1987.

[13] T. Matsumoto, L. O. Chua, and M. Komuro, "The double scroll," *IEEE Trans. Circuits Syst.*, vol. CAS-32, pp. 797–818, Aug. 1985.
[14] T. Matsumoto, L. O. Chua, and K. Tokumasu, "Double scroll via a two-transistor circuit," *IEEE Trans. Circuits Syst.*, vol. CAS-33, pp. 828–835, Aug. 1986.
[15] T. S. Parker and L. O. Chua, "The dual double scroll equation," to appear in *IEEE Trans. Circuits Syst.*, vol. CAS-34, no. 9, Sept. 1987.
[16] L. O. Chua and P. M. Lin, *Computer-Aided Analysis of Electronic Circuits: Algorithms and Computational Techniques.* Englewood Cliff, NJ: Prentice-Hall, 1975.
[17] B. Mandelbrot, *The Fractal Geometry of Nature.* New York, NY: Freeman, 1983.
[18] O. E. Rössler, "Continuous chaos-four prototype equations," *Ann. N.Y. Acad. Sci.*, vol. 31, pp. 376–392, 1979.
[19] C. T. Sparrow, "Chaoss in a three-dimensional single-loop feedback system with a piecewise-linear feedback function," *J. Math. Anal. Appl.*, vol. 83, pp. 275–291, 1981.

Shuxian Wu was born in Beijing, China, on October 2, 1957. She received the B.S. degree in electrical engineering from the Beijing Normal University in 1982 and the M.S. degree from the same university in 1985.

She has served as Assistant Professor at the Beijing Normal University since 1985. Her research interests include nonlinear dynamics and chaotic systems on which she has published several papers.

Chaos in Electronic Circuits

TAKASHI MATSUMOTO, FELLOW, IEEE

Invited Paper

*This paper describes three **extremely simple** electronic circuits in which chaotic phenomena have been observed. The simplicity of the circuits allows one to*

i) build them easily,
ii) confirm the observed phenomena by digital computer simulation, and in some cases
iii) rigorously prove the circuit is indeed chaotic.

A consequence of i) is that the interested reader can build, and then see and even listen to chaos.

*It is to be emphasized that these circuits are **not** analog computers. They are real physical systems.*

I. INTRODUCTION

Until recently, very few electrical engineers questioned the validity of the following statements:

> oscillation = periodic
>
> and
>
> noise = nondeterministic

Now it is undeniable that both of them are false. The purpose of this paper is to provide the reader with not only the circumstantial evidence which has lead to questions about the validity of these statements but also a rigorous proof for it. The evidence all comes from *extremely simple* electronic circuits which even high school students can build. No delicate and/or expensive equipment is necessary. It is strongly recommended that the interested reader build the circuits, and then *see* and even *listen* to the phenomena. It would be a lot of fun.

The circumstancial evidence shows that

> there is no reason why oscillation should be
>
> always periodic   (1.1)
>
> and that
>
> noise can come from a deterministic circuit.   (1.2)

Hands-on experience with those circuits tells us that

> there are low-order deterministic (Newtonian)
>
> systems which are *"unpredictable"*   (1.3)

in the sense that even an extremely small change of the initial condition eventually gives rise to an entirely different trajectory. The periodic oscillators are *"predictable"* in that every trajectory eventually converges to the same periodic orbit irrespective of the initial condition. Experience also shows that

> those systems in (1.3) can produce *"deterministic noise."*
>
> (1.4)

So far, the word *"chaos"* has been intentionally avoided because there has been no unanimously accepted definition of it. If one definition were used, there would be some inconsistency, while if another were used, there would be some inconvenience, and so forth. Therefore by a "chaotic" circuit in this paper is meant, more or less ambiguously, a circuit which admits a nonperiodic oscillation.

Given the extremely short period of time alloted for the preparation of this paper, it will have to be restricted to those circuits studied by the author and his colleagues, even though had it been possible, chaotic circuits studied by other people would have been included.

There will be three circuits described:

I) double scroll
II) folded torus
III) driven *R–L*-Diode.

The first two are autonomous while the third one is non-autonomous. The following format will be used to describe each circuit:

A) circuitry
B) experimental observations
C) confirmation
D) analysis
E) bifurcations.

Throughout the paper, the reader's attention is directed to the simplicity of these circuits, which allows one to

i) build them easily
ii) confirm observed phenomena by computer simulation easily and, in some cases
iii) rigorously prove the circuit is indeed chaotic.

It should be emphasized that the circuits discussed in this paper are *not* analog computers. In the circuits discussed below, the voltage and current of each circuit element play critical roles in the dynamics, while in an analog computer, only the node voltages of integrators are involved in the dynamics.

II. THE DOUBLE SCROLL

The circuit to be described in this section is one of the very few physical systems which fullfil i), ii), and iii) of the last section.

A. Circuitry

The circuitry is given in Fig. 1(a). It contains *only one nonlinear element*: a piecewise-linear resistor with *only two break points* given in Fig. 1(b). This circuit can be easily real-
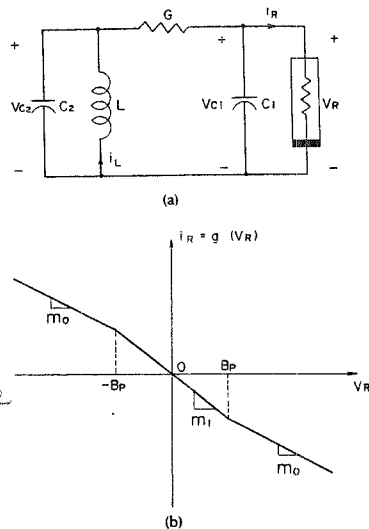
(a)

(b)

Fig. 1. A simple autonomous circuit with a chaotic attractor. (a) The circuitry. (b) v–i characteristic of the nonlinear resistor.

B. Experimental Observations

Fig. 3(a), (b), and (c) shows a trajectory *projected* onto the (i_L, v_{C_1})-plane, (i_L, v_{C_2})-plane, and (v_{C_1}, v_{C_2})-plane, respectively, at the following parameter values:

$$C_1 = 0.0053 \ \mu F \quad C_2 = 0.047 \ \mu F \quad L = 6.8 \ mH$$
$$R = 1.21 \ k\Omega \quad R_B = 56 \ k\Omega \quad R_1 = 1 \ k\Omega$$
$$R_2 = 3.3 \ k\Omega \quad R_3 = 88 \ k\Omega \quad (2.1)$$
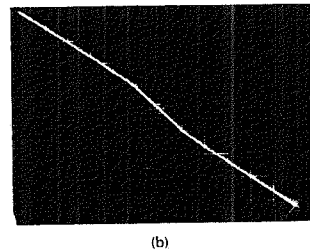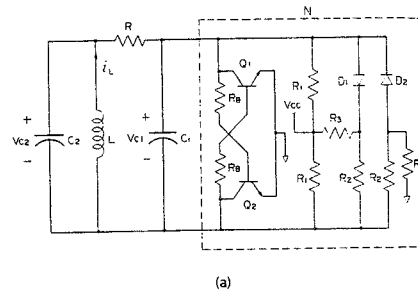$$R_4 = 39 \ k\Omega \quad V_{cc} = 29 \ V.$$

(a)

(b)

Fig. 2. A realization of the circuit in Fig. 1. (a) Circuitry. Q_1, Q_2 = 2SC1815, D_1, D_2 = 1S1588. (b) Measured v–i characteristic of N. Horizontal scale: 5 V/div. Vertical scale: 1 mA/div.

Of course, they are the *nominal* values; the exact values could fall within 10 percent of these due to component tolerances. The photographs indicate that the solution trajectory is nonperiodic. In fact, the time waveforms of $v_{C_1}(t)$, $v_{C_2}(t)$, and $i_L(t)$ look like noise (Fig. 4(a), (b), and (c), respectively).

C. Confirmation

The dynamics of the circuit in Fig. 1 is governed by

$$C_1 \frac{dv_{C_1}}{dt} = G(v_{C_2} - v_{C_1}) - g(v_{C_1})$$

$$C_2 \frac{dv_{C_2}}{dt} = G(v_{C_1} - v_{C_2}) + i_L$$

$$L \frac{di_L}{dt} = -v_{C_2} \qquad (2.2)$$

where $g(\cdot)$ represents the piecewise-linear characteristic of the resistor given by Fig. 1(b).

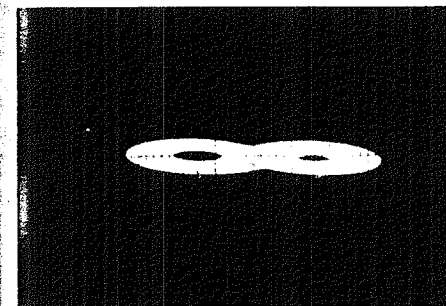The experimental observations are confirmed by solving (2.2) with the following rescaled parameter values:[1]

$$1/C_1 = 9 \quad 1/C_2 = 1 \quad 1/L = 7 \quad G = 0.7,$$
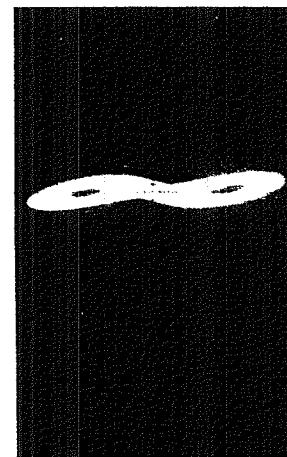$$m_0 = -0.5 \quad m_1 = -0.8 \quad B_p = 1. \qquad (2.3)$$

[1]Of course, one can make the confirmation via the circuit of Fig. 2 by using an accurate model of the transistors, e.g., SPICE 2 [2].
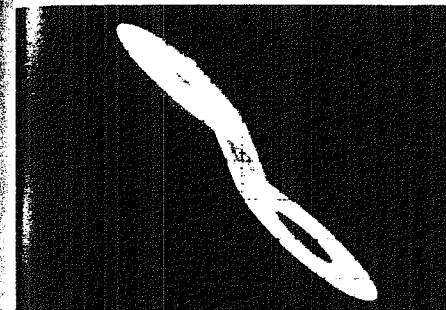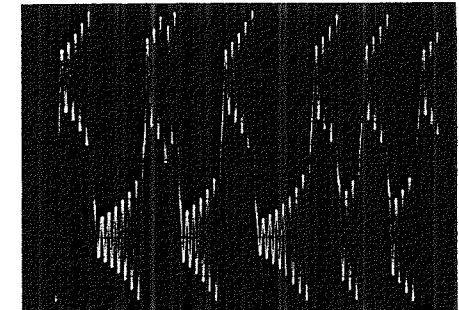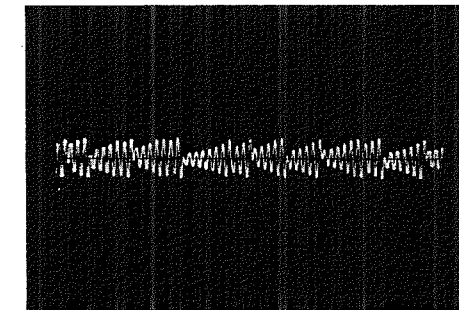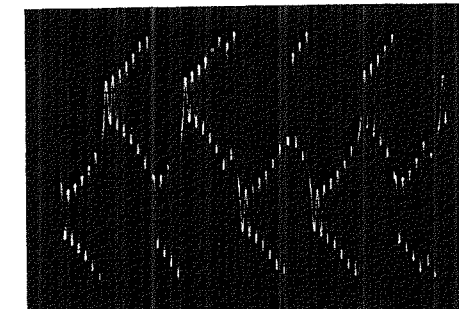
(a)

(b)

(c)

Fig. 3. Observed attractor. Voltage: 2 V/div. Current: 2 mA/div. (a) Projection onto the (i_L, v_{C_1})-plane. (b) Projection onto the (i_L, v_{C_2})-plane. (c) Projection onto the (v_{C_1}, v_{C_2})-plane.

(a)

(b)

(c)

Fig. 4. Measured time waveforms. Horizontal scale: 1 ms/div. (a) $v_{C_1}(t)$. Vertical scale: 2 V/div. (b) $v_{C_2}(t)$. Vertical scale: 2 V/div. (c) $i_L(t)$. Vertical scale: 2 mA/div.

The results are given in Fig. 5(a), (b), and (c). The broken line curve indicates a *saddle-type*[2] periodic orbit which will be explained later. There is a large periodic attractor outside the nonperiodic attractor *and* the saddle-type periodic orbit due to the *eventual passivity* of the transistors [1]. Note that one can replace the two transistors with one operational amplifier, as given in Fig. 6. To the interested reader

[2]There is an unstable direction as well as a stable direction. Therefore, one cannot see a saddle-type periodic orbit on the oscilloscope.
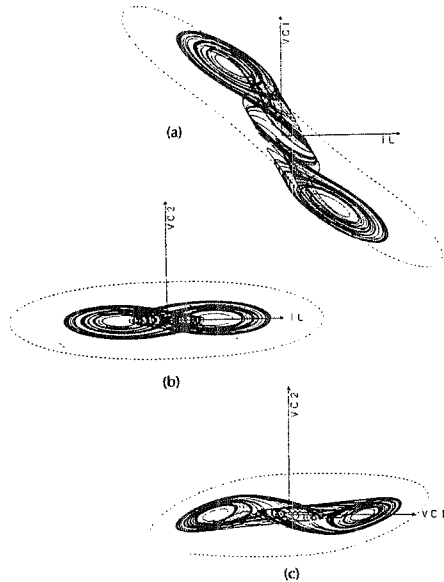
ized, for example, by the circuit of Fig. 2(a), where the subcircuit N enclosed by the broken line realizes the piecewise-linear resistor. Fig. 2(b) shows the measured v–i characteristic of N.

(a)

(b)

(c)

Fig. 5. Confirmation. (a) Projection onto the (i_L, v_{C_1})-plane. (b) Projection onto the (i_L, v_{C_2})-plane. (c) Projection onto the (v_{C_1}, v_{C_2})-plane.
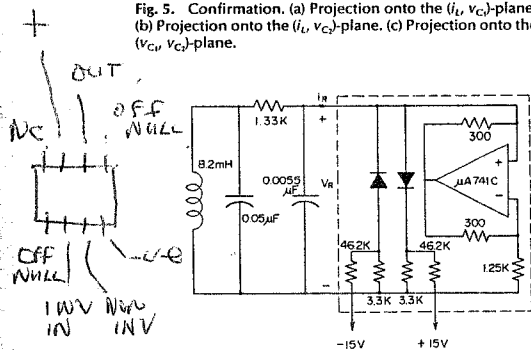

Fig. 6. Another realization of the circuit in Fig. 1.

who wants to build the circuit, Fig. 6 is recommended, because, first, the symmetry of the v–i characteristic can be realized easily without worrying about the pair (Q_1, Q_2), and, second, the battery voltage is less than that of Fig. 2.

Fig. 7 gives the power spectrum of $v_{C_1}(t)$, which indicates a broad-band continuous power spectrum. Because most of the frequency components are within the **audible** frequencies, one can listen to the sound, which is mysterious and amusing. It is strongly recommended that the reader listen to it. It is a lot of fun.[3]

[3]As there have been many requests for the real circuit, we have produced many circuits illustrated in Fig. 6. The interested reader can write to the author.
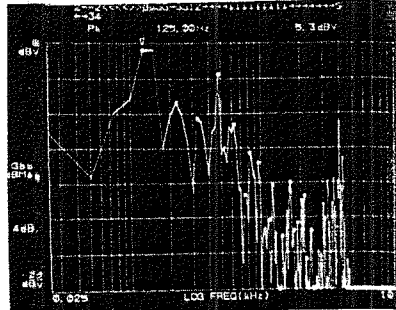

Fig. 7. Power spectrum of $v_{C_1}(t)$.

Let us give several circuit-theoretic explanations of the chaotic behavior of this circuit. First note that the parallel connection (tank circuit) of C_2 and L constitutes one basic oscillatory mechanism in the (v_{C_2}, i_L)-plane, whereas the conductance G provides the interactions between the (C_2, L)-oscillatory component and the *active* resistor $g(\cdot)$ together with C_1. This active resistor is responsible for the circuit's chaotic behavior. If this resistor were *locally passive*, it is well known that the circuit would be quite tame; all solutions would approach a globally asymptotically stable equilibrium. Since $g(\cdot)$ is always *locally active*, i.e., $v_R(t)\, i_R(t) < 0$ (except at the origin) it keeps supplying power to the external circuit. The attracting nature of the chaotic trajectories comes from the power dissipation in the *passive* element G, thereby restraining its growth. The *power balance*, however, is rather delicate, and varies continuously with time, never repeating itself periodically.

D. Analysis

Because of the simplicity of (2.2), one can perform a *rigorous* analysis. In order to simplify the analysis, we transform (2.2) into

$$
\begin{cases}
\dfrac{dx}{dt} = \alpha(y - h(x)) \\[2mm]
\dfrac{dy}{dt} = x - y + z \\[2mm]
\dfrac{dz}{dt} = -\beta y
\end{cases} \tag{2.4}
$$

$$
h(x) = \begin{cases}
bx + a - b, & x \geq 1 \\
ax, & |x| \leq 1 \\
bx - a + b, & x \leq -1
\end{cases} \tag{2.5}
$$

via

$$
x = v_{C_1}/B_p \quad y = v_{C_2}/B_p \quad z = i_L/(B_p G)
$$
$$
\tau = tG/C_2 \quad a = m_1/G + 1 \quad b = m_0/G + 1
$$
$$
\alpha = C_2/C_1 \quad \beta = C_2/(LG^2). \tag{2.6}
$$

Here, we have abused our notation for time: it should have been "τ" instead of "t." There will be no confusion,

however. Note that $h(x)$ includes both x and $g(x)$. We begin with the following observations:

i) Equation (2.4) is symmetric with respect to the origin, i.e., the vector field is invariant under the transformation

$$(x, y, z) \to (-x, -y, -z).$$

ii) Consider the equilibria

$$
\begin{cases}
h(x) = 0 \\
y = 0 \\
x + z = 0.
\end{cases}
$$

It follows from the form of $h(\cdot)$ that (2.4) has a unique equilibrium in each of the following three subsets of $\mathbb{R}^3$:

$$
\begin{aligned}
D_1 &= \{(x, y, z): x \geq 1\} \\
D_0 &= \{(x, y, z): |x| \leq 1\} \\
D_{-1} &= \{(x, y, z): x \leq -1\}
\end{aligned}
$$

provided that $a, b \neq -1$. The equilibria are explicitly given by

$$
\begin{aligned}
P^+ &= (k, 0, -k) \in D_1 \\
0 &= (0, 0, 0) \in D_0 \\
P^- &= (-k, 0, k) \in D_{-1}
\end{aligned}
$$

where $k = (b - a)/(b + 1)$.

iii) In each of D_1, D_0, and D_{-1}, (2.4) is linear. In fact, letting

$$
x = (x, y, z) \quad k = (k, 0, -k)
$$

and introducing the 3×3 real matrix

$$
A(\alpha, \beta, c) = \begin{bmatrix}
-\alpha c & \alpha & 0 \\
1 & -1 & 1 \\
0 & -\beta & 0
\end{bmatrix}
$$

where A depends on α, β, and a parameter c, which is equal to a in D_0, and b in D_1 and D_{-1}. We can recast (2.4) as follows:

$$
\frac{dx}{dt} = \begin{cases}
A(\alpha, \beta, b)(x - k), & x \in D_1 \\
A(\alpha, \beta, a)x, & x \in D_0 \\
A(\alpha, \beta, b)(x + k), & x \in D_{-1}
\end{cases}
$$

The set of parameter values (α, β, a, b) corresponding to (2.3) is given (via 2.6)) by

$$(\alpha, \beta, a, b) = (9, 14\tfrac{2}{7}, -\tfrac{1}{7}, \tfrac{2}{7}).$$

Then the matrix

$$A_1 = A(9, 14\tfrac{2}{7}, \tfrac{2}{7})$$

associated with the regions D_1 and D_{-1} has a real eigenvalue[4]

$$\tilde{\gamma}_1 \approx -3.94$$

and a pair of complex-conjugate eigenvalues

$$\tilde{\sigma}_1 \pm j\tilde{\omega}_1 \approx 0.19 \pm j3.05.$$

Similarly, the matrix

$$A_0 = A(9, 14\tfrac{2}{7}, -\tfrac{1}{7})$$

[4]The tilde is used here to distinguish the eigenvalues from the "normalized" eigenvalues which will be defined later.

associated with the region D_0 has a real eigenvalue

$$\tilde{\gamma}_0 \approx 2.22$$

and a pair of complex-conjugate eigenvalues

$$\tilde{\sigma}_0 \pm j\tilde{\omega}_0 \approx -0.97 \pm j2.71.$$

Let $E^r(P^\pm)$ be the eigenspace corresponding to the real eigenvalue $\tilde{\gamma}_1$ at $P^\pm$ and let $E^c(P^\pm)$ be the eigenspace corresponding to the complex eigenvalues $\tilde{\sigma}_1 \pm j\tilde{\omega}_1$ at $P^\pm$. Similarly, let $E^r(0)$ and $E^c(0)$ be the eigenspaces corresponding to $\tilde{\gamma}_0$ and $\tilde{\sigma}_0 \pm j\tilde{\omega}_0$, respectively. Then the eigenspaces are given explicitly by the following equations:

$$E^r(P^\pm): \quad \frac{x \mp k}{\tilde{\gamma}_1^2 + \tilde{\gamma}_1 + \beta} = \frac{y}{\tilde{\gamma}_1} = \frac{z \pm k}{-\beta}$$

$$E^c(P^\pm): \quad (\tilde{\gamma}_1^2 + \tilde{\gamma}_1 + \beta)(x \mp k) + \alpha\tilde{\gamma}_1 y + \alpha(z \pm k) = 0$$

$$E^r(0): \quad \frac{x}{\tilde{\gamma}_0^2 + \tilde{\gamma}_0 + \beta} = \frac{y}{\tilde{\gamma}_0} = \frac{z}{-\beta}$$

$$E^c(0): \quad (\tilde{\gamma}_0^2 + \tilde{\gamma}_0 + \beta)x + \alpha\tilde{\gamma}_0 y + \alpha z = 0.$$

Relative positions of the eigenspaces and related sets are described in Fig. 8, where

$$
\begin{aligned}
L_0 &= E^c(0) \cap U_1 & C &= E^r(0) \cap U_1 \\
L_1 &= E^c(P^+) \cap U_1 & D &= E^r(P^+) \cap U_1 \\
L_2 &= \{x \in U_1 : \xi(x)//U_1\} & E &= L_0 \cap L_2 \\
A &= L_0 \cap L_1 & F &= \{x \in L_2 : \xi(x)//L_2\}. \\
B &= L_1 \cap L_2
\end{aligned}
$$

Here $\xi(x)//L_2$ means that the vector field $\xi(x)$ defined by (2.4) is in parallel with L_2.

Since the dynamics is *piecewise-linear*, this picture (Fig. 8) already illustrates a great deal of important information as described in the following subsection.

1) Geometric Structure: Let us describe the structure of the attractor. In this subsection, we will use the following notation for the eigenspaces:

$$
\begin{aligned}
E^s(P^\pm) &= E^r(P^\pm) & E^u(P^\pm) &= E^c(P^\pm) \\
E^s(0) &= E^c(0) & E^u(0) &= E^r(0).
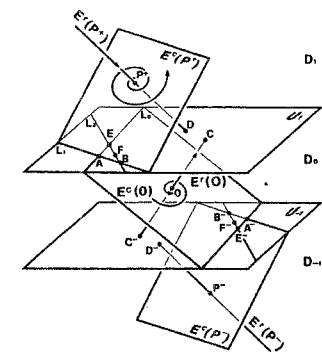\end{aligned}
$$

Fig. 8. Eigenspaces of the equilibria and related sets.

Let φ^t be the flow generated by (2.4) and pick an initial condition $x_0 \in E^u(P^+)$ in a neighborhood of P^+. Then, for $t > 0$, the flow $\varphi^t(x_0)$ starts wandering away from P^+ on $E^u(P^-)$. After winding round P^+ several times in a counterclockwise direction, it hits the plane U_1 at some time, say $t_1 : x_1 = \varphi^{t_1}(x_0)$. The trajectory up to t_1 is a spiral because (2.4) is linear in D_1 and $E^u(P^+)$ is invariant. Clearly, $x_1 \in L_0$. Note that the line L_2 is a straight line parallel to the z-axis because $\dot{x}$ is independent of z. Observe that L_2 separates the plane U_1 into two regions, one (to which A belongs) where $\dot{x} < 0$ and another where $\dot{x} > 0$. Since $\varphi^t(x_0)$ hits the plane U_1 downward (recall that the motion is counterclockwise) at $t = t_1$, one sees that x_1 belongs to the line segment $\overline{GB}$, where G is a point on L_0 to the left of and sufficiently far from A, i.e., $\dot{x} < 0$ at x_1. The "fate" of $\varphi^t(x_1)$ depends crucially on which part of $\overline{GB}$ x_1 lies (see Fig. 9).

Case 1: $x_1 = A$ (red):

Since the dynamics is linear in D_0, one can check analytically that $\varphi^t(A)$ never hits U_{-1} directly for the parameter values (2.3), i.e., the real part $\bar{\sigma}_0$ of the complex conjugate eigenvalues is negative and small compared to the imaginary part $\bar{\omega}_0$. Since $A \in E^s(0)$ and since $E^s(0)$ is invariant, $\varphi^t(x_1)$ approaches the origin asymptotically as $t \to \infty$ (see Fig. 9). The trajectory is a spiral with an infinite number of rotations for (2.4) is linear in D_0 and $E^s(0)$ is invariant.

Case 2: $x_1 \in$ Interior $\overline{AB}$ (blue):

In this case $\varphi^t(x_1)$ has two components in the sense that its projection onto $E^s(0)$ approaches the origin asymptotically and its projection onto $\overline{0C} \subset E^u(0)$ wanders away from the origin. This means that $\varphi^t(x_1)$ moves up along a spiral with the central axis $\overline{0C}$ and then eventually hits U_1 again from below: $x_2 = \varphi^{t_2}(x_1)$. The number of rotations of $\varphi^t(x_1)$

around $\overline{0C}$ can get arbitrarily large without bounds if x_1 very close to A. These processes naturally give rise to th map

$$\Psi: \overline{AB} \to U_1$$

defined by

$$\Psi(x_1) = x_2.$$

The image $\Psi(\overline{AB})$ is a spiral with the center at C which is tangent to L_0 at B. After hitting U_1, the trajectory $\varphi^t(x_2)$ has two components in the sense described above: one which stays in $E^u(P^+)$ and moves away from P^+ in a spiral manner and another in $E^s(P^+)$ which approaches P^+ asymptotically. Therefore, $\varphi^t(x_2)$ ascends in a spiral path with the central axis $\overline{DP^+}$ and flattens itself onto $E^u(P^-)$ from below (see Fig. 9).

Case 3: $x_1 \in$ Interior $\overline{GA}$ (green):

$\varphi^t(x_1)$ has two components in the same sense as above. One component stays in $E^s(0)$ and asymptotically approaches 0 in a spiral manner. Another component stays in $E^u(P^+)$ and moves away from 0 on $\overline{0C^-}$. This means that $\varphi^t(x_1)$ descends along a spiral with the central axis $\overline{0C^-}$, hits U_{-1} at $x_2 = \varphi^{t_2}(x_1)$, and eventually enters region D_{-1}. The closer x_1 is to point A, the larger the number of rotations of $\varphi^t(x_1)$ around $\overline{0C^-}$. After entering into D_{-1}, the flow $\varphi^t(x_2)$ consists of two components: one which is in $E^u(P^-)$ and moves away from P^-, and another which stays in $E^s(P^-)$ and asymptotically approaches P^-. Therefore, $\varphi^t(x_2)$ descends spirally with the central axis $\overline{D^-P^-}$ and eventually flattens itself onto $E^u(P^-)$ from above (see Fig. 9).

Based upon the above observations, we can understand the geometric structure of the attractor. Fig. 10 describes the structure after several simplifications. Note that two
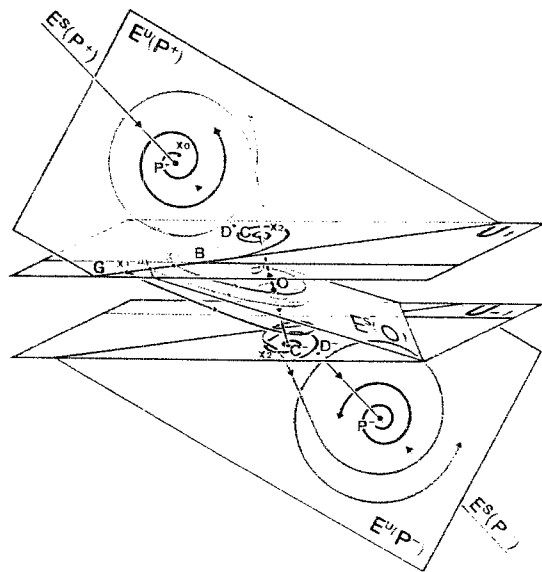

Fig. 9. Typical trajectories.

Fig. 10. A geometric model of the double scroll.

sheet-like objects are curled up together into spiral forms: these form the "double scroll."

Let us look at a cross section of the attractor. Fig. 11 gives the cross section at $v_{C_1} = 0$, where the double-scroll structure is clearly seen.
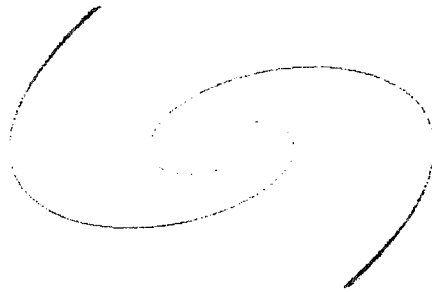

Fig. 11. Cross section of the double scroll at $v_{C_1} = 0$.

Finally, the *Lyapunov exponents* [4] turn out to be

$$\mu_1 \approx 0.23 \quad \mu_2 \approx 0 \quad \mu_3 \approx -1.78$$

so that the *Lyapunov dimension* is

$$d_L = 2 + (\mu_1 + \mu_2)/|\mu_3| \approx 2.13.$$

This is a fractal between 2 and 3 and agrees with the observed sheet-like structure.

2) Homoclinicity: One can take full advantage of the piecewise-linearity of (2.4) and *prove* that it is chaotic in the sense of Shilnikov. To begin with, recall that the line L_2 denotes the set of points where the trajectory of (2.4) is *tangent* to U_1. On the left-hand side of L_2, a trajectory hits U_1 *downward*, while on the right-hand side of L_2, a trajectory hits U_1 *upward*. Consider the trajectory starting with **0** on $E^c(0)$, the unstable eigenvector. It reaches point C, which is the intersection of the unstable eigenspace of **0** with U_1. *If* the trajectory starting from C hits a point on the line segment $\overline{AE}$ at some time, say (Fig. 12)

$$\varphi^{t_1}(C) \in \overline{AE} \tag{2.7}$$
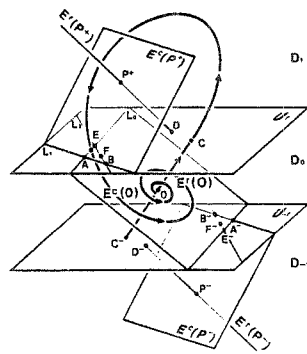

Fig. 12. Homoclinic trajectory at the origin.

where φ^t is the flow generated by (2.4), then the trajectory would stay on $E^c(0)$ and asymptotically approach **0**, because $E^c(0)$ is *invariant*. Such a trajectory is called **homoclinic** and it is related to a very complicated behavior of solutions to differential equations. A rigorous statement is given by the following theorem of Shilnikov ([3]–[5]):

Theorem (Shilnikov)
Consider

$$\frac{dx}{dt} = f(x)$$

where $f: \mathbb{R}^3 \to \mathbb{R}^3$ is continuous and piecewise-linear. Let the origin be an equilibrium with a real eigenvalue $\gamma > 0$ and a complex conjugate pair $\alpha \pm j\omega$ ($\alpha < 0$, $\omega \neq 0$). If

i) $|\alpha| < \gamma$, and
ii) there is a *homoclinic* orbit through the origin

then there is a **horseshoe** near the homoclinic orbit. ☐

The horseshoe mentioned in the theorem is formed in the following manner. Consider Fig. 13, where an appropriate coordinate system is chosen so that the unstable eigenspace corresponds to the z-axis and the stable eigenspace corresponds to the (x, y)-plane. One can take an
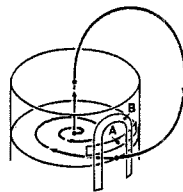

Fig. 13. The horseshoe embedded near the homoclinic trajectory.

appropriate cylinder and a narrow strip on the surface of the cylinder such that its Poincaré return image is strongly contracted in the horizontal direction, strongly stretched in the vertical direction, and then bent as depicted in Fig. 13. It should be noted that a rectangle like A returns to the long thin object B. The horseshoe thus formed gives rise to an extremely complicated behavior. Namely, a horseshoe has a positively *and* negatively invariant set Λ such that [4]

i) Λ is a Cantor set,
ii) Λ contains a countable number of *saddle-type* periodic orbits of arbitrarily long periods,
iii) Λ contains an *uncountable* number of *bounded nonperiodic* orbits, and
iv) Λ contains a dense orbit.

Moreover, a horseshoe is *structurally stable*, i.e., small perturbations *do not* destroy i)–iv).

Therefore, if a horseshoe is embedded somewhere in the dynamics, the trajectory will be extremely complicated. In fact, those who have experience in this area would suspect, that wherever there is chaos, a horseshoe is embedded in the vicinity of a homoclinic orbit (or a heteroclinic orbit).

3) Proof of Chaos: One can prove rigorously [6], [7] that this circuit is chaotic in the sense of Shilnikov.

Theorem
Consider (2.4) and (2.5) and fix

$$\alpha = 7 \quad a = -\tfrac{1}{7} \quad b = \tfrac{2}{7}.$$

Then there is a $\beta \in [6.5, 10.5]$ such that **the circuit is chaotic** in the sense of Shilnikov.

Let us briefly describe how one can *prove* this. Recall that what one wants to prove is (2.7). This, however, is extremely difficult, for one has to compute the *return time*, t_1, at which a trajectory hits the plane U_1. In general, it is *impossible* to compute t_1 analytically, because the trajectory $\varphi^{t_1}(C)$ involves sin, cos, and exp, and therefore, t_1 is defined only implicitly by a **transcendental equation**. In order to overcome this difficulty, we will make the following change of coordinate systems (Fig. 14):

a) Take a map $\Psi_1: \mathbb{R}^3 \to \mathbb{R}^3$ such that

$$\Psi_1(P^+) = 0$$

$$\Psi_1(U_1) = V_1 = \{(x, y, z): x + z = 1\}$$

$$\frac{1}{\bar{\omega}_1} D\Psi_1(\xi(\Psi_1^{-1}x)) = \xi_1(x) = \begin{bmatrix} \sigma_1 & -1 & 0 \\ 1 & \sigma_1 & 0 \\ 0 & 0 & \gamma_1 \end{bmatrix} x \tag{2.8}$$

where $\sigma_1 = \bar{\sigma}_1/\bar{\omega}_1$ and $\gamma_1 = \bar{\gamma}_1/\bar{\omega}_1$ and D denotes a derivative.
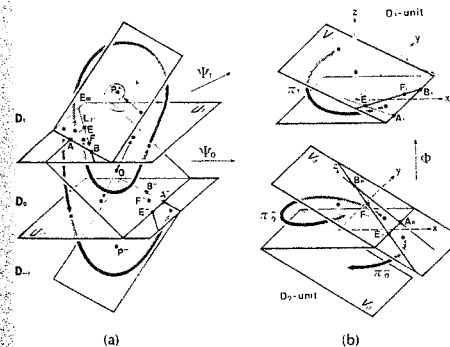

Fig. 14. Geometrical structure and typical trajectories of the original piecewise-linear system and their images in the D_0-unit and D_1-unit of the transformed system. (a) Original system and typical trajectories. (b) D_0-, D_1-units and half-return maps.

b) Take a map $\Psi_0: \mathbb{R}^3 \to \mathbb{R}^3$ such that

$$\Psi_0(0) = 0$$

$$\Psi_0(U_1) = V_0 = \{(x, y, z): x + z = 1\}$$

$$\Psi_0(U_{-1}) = V_0^- = \{(x, y, z): x + z = -1\}$$

$$\frac{1}{\bar{\omega}_0} D\Psi_0(\xi(\Psi_0^{-1}x)) = \xi_0(x) = \begin{bmatrix} \sigma_0 & -1 & 0 \\ 1 & \sigma_0 & 0 \\ 0 & 0 & \gamma_0 \end{bmatrix} x \tag{2.9}$$

---

where $\sigma_0 = \bar{\sigma}_0/\bar{\omega}_0$ and $\gamma_0 = \bar{\gamma}_0/\bar{\omega}_0$. We will call the transformed systems (2.8) and (2.9), the D_1-unit and D_0-unit, respectively.

In order to make the transformed differential equation consistent, one has to "match" (2.8) with (2.9) through the map

$$\Phi = (\Psi_1|U_1) \circ (\Psi_0|U_1)^{-1} \tag{2.10}$$

where $\Psi_1|U_1$ (resp., $\Psi_0|U_1$) denotes the restriction of Ψ_1 (resp., Ψ_0) to U_1. These maps can be explicitly given in terms of the eigenvalues.

Consider the **negative half return map** (Fig. 14) in the D_1-unit defined by

$$\pi_1(x) = \varphi_1^{-T}(x), \quad x \in V_1 \tag{2.11}$$

where φ_1^{-T} is the flow in the D_1-unit and

$$T = \inf \{t > 0: \varphi_1^{-T}(x) \in V_1\}. \tag{2.12}$$

Now the homoclinicity condition (2.7) can be expressed as

$$\boxed{C_1 \in \pi_1(\overline{A_1 E_1})} \tag{2.13}$$

where

$$C_1 = \Psi_1(C) \quad A_1 = \Psi_1(A) \quad E_1 = \Psi_1(E).$$

Although the transformed flow φ_1^{-T} has a simpler expression (recall (2.8)) than the original flow φ^T, the half return time, T, defined by (2.12) is *still* a solution to a transcendental equation. The following proposition, however, provides us with a breakthrough.

Proposition 2.1

$$\pi_1(\overline{A_1 E_1}) = \left\{ e^{-\sigma_1 \tau} \begin{bmatrix} \cos \tau & \sin \tau \\ -\sin \tau & \cos \tau \end{bmatrix} \right.$$
$$\cdot \left(\frac{\langle \varphi_1^{-\tau}(E_1), h \rangle - 1}{\langle \varphi_1^{-\tau}(E_1 - A_1), h \rangle} A_1 \right.$$
$$\left. \left. - \frac{\langle \varphi_1^{-\tau}(A_1), h \rangle - 1}{\langle \varphi_1^{-\tau}(E_1 - A_1), h \rangle} E_1 \right) \middle| \tau > 0 \right\}.$$
$$\tag{2.14}$$

where $h = (1, 0, 1)$.

Formula (2.14) says that in order to obtain the π_1-image of $\overline{A_1 E_1}$, one *does not* have to compute the half return times. Rather, (2.14) uses τ as a *parametrization* of $\pi_1(\overline{A_1 E_1})$. It follows immediately from (2.14) that $\pi_1(\overline{A_1 E_1})$ is a *shrinking spiral*. Fig. 15 shows the V_1-plane. The curve $\widehat{E_1 A_1'}$ is a part of $\pi_1(\overline{A_1 E_1})$. Several other points and curves are also drawn. They are unnecessary for the present purpose, however. The reader is referred to [6].

Let us look at Fig. 16 which is the V_1-plane, again. Consider the annulus region bounded by two circles S_a and S_b. The radius of S_a is the distance of A_1 from the origin, while the radius of S_b is $\|E_1\| e^{-2\pi\sigma_1}$. One can prove [6], then, that the part $\widehat{E_1 ee'}$ of $\pi_1(\overline{E_1 A_1})$ is *trapped* within the annulus region for all $\beta \in [6.5, 10.5]$.

Proposition 2.2 [6]

i) C_1 is a continuous function of $\beta \in [6.5, 10.5]$.
ii) Let $C_1 = (x_C, y_C)$. Then $y_C > 0$ and there is an x_E such that $x_C < x_E < 1$ for $\beta \in [6.5, 10.5]$. ☐
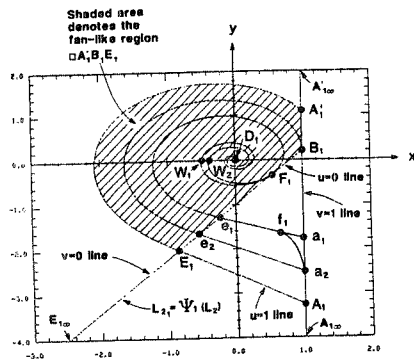
Fig. 15. V_1-plane. $\widehat{F_1 W_1 D_1} = \pi_1(\widehat{F_1 B_1})$. $\widehat{e_1 F_1 W_2 D_1} = \pi_1(\widehat{e_1 a_1})$. $\widehat{e_2 B_1} = \pi_1(\widehat{e_2 a_2})$. $\widehat{E_1 A_1'} = \pi_1(\widehat{e_2 a_2})$, and $f_1 = \pi_1^{-1}(F_1)$. The position of f_1 is exaggerated in this figure for clarity. The actual position of f_1 is very close to a_1.
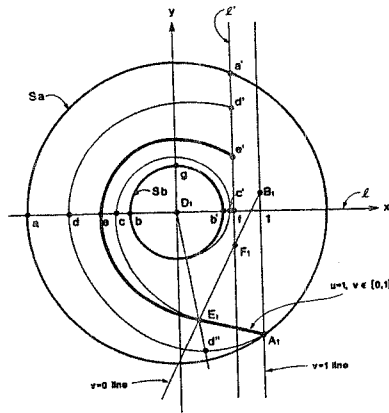

Fig. 16. The annulus region bounded by S_a and S_b.

Finally, *if*

$$\begin{cases} C_1 \ (\beta = 6.5) \text{ is outside of } S_a \\ \text{and} \\ C_1 \ (\beta = 10.5) \text{ is inside of } S_b \end{cases} \quad (2.15)$$

then *Proposition 2.2* ensures that

$$\{C_1 | \beta \in [6.5, 10.5]\}$$

is a simple curve and it *intersects* with $\pi_1(\overline{A_1 E_1})$ somewhere in the annulus region: *homoclinicity*. The final step, therefore, is to prove (2.15). In order to do this, a **computer-assisted proof** is performed.

4) Computer-Assisted Proof of (2.15): Statements in (2.15) can be written as

$$\beta = 6.5: \ \|C_1\| > \|A_1\|$$

$$\beta = 10.5: \ \|C_1\| < \|E_1\| e^{-2\pi\sigma_1}$$

---

where σ_1 is defined in (2.8), the real part of the complex conjugate eigenvalues at $P^\pm$ "normalized" by the imaginary part. The projections of A_1, C_1, and E_1 onto V_1 can be explicitly given in terms of the eigenvalues

$$A_1 = (1, p_1) \qquad C_1 = (x_C, y_C)$$

and

$$E_1 = (x_E, y_E)$$

where

$$x_C = 1 - \frac{(\sigma_1^2 + 1)[(\sigma_0 + \gamma_0 k_1)^2 + 1]}{(\sigma_0^2 + 1)Q_1}$$

$$y_C = \frac{\gamma_1[1 - \sigma_1(\sigma_1 - \gamma_1)]}{Q_1} - \frac{(\sigma_1^2 + 1)\gamma_0 k_1}{(\sigma_0^2 + 1)\gamma_1 Q_1}$$
$$\cdot \{k_1\gamma_0[\sigma_1(\sigma_1 - \gamma_1) + 1] + 2\sigma_0\gamma_1(\sigma_1 - \gamma_1)\}$$

$$p_1 = \sigma_1 + k_1(\sigma_1^2 + 1)/\gamma_1, \quad k_1 = -\gamma_1/\gamma_0$$

$$Q_1 = (\sigma_1 - \gamma_1)^2 + 1$$

$$x_E = \gamma_1(\gamma_1 - \sigma_1 - p_1)/Q_1$$

$$y_E = \gamma_1[1 - (\sigma_1 - \gamma_1)]/Q_1.$$

The eigenvalues, in turn, are a function of β. The real eigenvalue $\tilde{\gamma}_i$, $i = 0, 1$, is a *real* solution to the characteristic equation

$$\tilde{\gamma}_i^3 + (\alpha c_i + 1)\tilde{\gamma}_i^2 + (\alpha c_i - \alpha + \beta)\tilde{\gamma}_i + \alpha\beta c_i = 0$$

where $c_0 = a$, $c_1 = b$. A simple calculation shows that the complex conjugate pair satisfy

$$\tilde{\sigma}_i = -(\alpha c_i + 1 + \tilde{\gamma}_i)/2$$

$$\tilde{\omega}_i^2 = -(\alpha c_i - 1 - \tilde{\gamma}_i)^2/4 - \alpha^2 c_i/(\tilde{\gamma}_i + \alpha c_i).$$

This means that given a β, one can compute A_1, C_1, and E_1 by finding zeros of polynomials of degree at most 3 and by performing the operations $+$, $-$, $\times$, and $\div$. *In principle*, this can be done by hand. However, it would be **formidably** tedious. The *computer-assisted proof* given in [7] *accurately* estimates the errors incurred by

i) finding a zero of a polynomial,
ii) $+$, $-$, $\times$, $\div$
iii) conversion of a real number to and from the corresponding machine represented number.

The last error needs to be taken care of, since a given decimal number may not be machine-representable. The program in [7] accurately gives a lower bound and an upper bound for every value involved. In particular

$$\beta = 6.5: \ \|C_1\|^2 \geq 2.003$$
$$> 1.557 \geq \|A_1\|^2 \quad (2.16)$$

$$\beta = 10.5: \ \|C_1\|^2 \leq 0.500$$
$$\|E_1\|^2 \geq 1.667 \quad (2.17)$$

In order to take care of $e^{-4\pi\sigma_1}$, we compute the bound

$$-4\pi\sigma_1 \leq -0.688$$

so that

$$e^{-1} < e^{-4\pi\sigma_1}.$$

---

cause $0 < e < 3$, we have

$$\|E_1\|^2 e^{-4\pi\sigma_1} > \|E_1\|^2/3 \geq 0.555. \quad (2.18)$$

This last inequality together with (2.17) gives the desired inequality, thereby proving the homoclinicity. Inequality i) of the Shilnikov theorem can be proved by the same program together with several analyses. □

Let us explain how the D_0-unit is related to the above argument. Recall Fig. 12, where we described a homoclinic trajectory. *A priori*, however, there is no guarantee that the trajectory, after hitting $\overline{A_1 E_1}$, should *not* hit U_{-1} directly, in which case the homoclinicity does not hold. In order to prove that would not happen for $\beta \in [6.5, 10.5]$, we need to take care of the D_0-unit where **positive half return maps are needed** [6]:

$$\pi_0^+ : U_1 \rightarrow U_1 \quad (2.19)$$

$$\pi_0^- : U_1 \rightarrow U_{-1}. \quad (2.20)$$

Let β^* be the value of β at the homoclinicity. It is very important to note that **even though a small change of β would destroy the homoclinicity, the horseshoe is still present,** because it is structurally stable. It is also worth noting that even though a small change in β may destroy this particular homoclinic trajectory (Fig. 12), there are *infinitely many* values of β near β^* which give rise to other types of homoclinicity. For example, a trajectory starting with **0** on $E'(0)$, comes back to a point very close to **0** but not exactly, makes another round and comes back exactly to **0** (see Fig. 17).
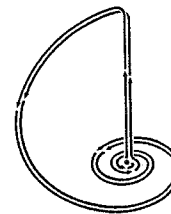

Fig. 17. Another homoclinicity.

Similarly, one can think of a homoclinic trajectory coming back to **0** after making three rounds, etc. [8]. A similar statement holds for heteroclinicity (see Section II-E7). Therefore, there is a great number of horseshoes in (2.4) which appears to explain why chaos has been observed.

Bifurcations

A rich variety of bifurcations has been observed from the circuit of Fig. 1. Fig. 18 shows the **two-parameter bifurcation diagram** in the (α, β)-plane, where $a = -\frac{1}{7}$ and $b = \frac{2}{7}$ are fixed. The two-parameter bifurcation diagram is generated by a rigorous bifurcation analysis described in [6] and [10] where the half return maps defined by (2.10), (2.19), and (2.20) are extensively used. In order to explain what the picture means, let us fix $\beta = 14\frac{2}{7}$ (recall that this is the original value in (2.3)) and vary $\alpha \geq 0$. This essentially corresponds to fixing a value of the inductance L while varying the value of C_1, where α and C_1 are inversely related: $\alpha = C_2/C_1$. In Fig. 18, for each numbered point in the (α, β)-plane, the trajec-

---

tory projected onto the (z, x)-plane, is depicted in the box with the corresponding number.

One can show [9], [10] that the origin is always unstable. The other equilibria, $P^\pm$, change their stability type depending on α. For a small value of $\alpha > 0$, for example, at ☐1 of Fig. 18, $P^\pm$ are stable and all the trajectories converge to one of them. Typical trajectories projected onto the (z, x)-plane $((i_L, v_{C_1})$-plane) are depicted in Box ☐1 in Fig. 18.

1) Hopf Bifurcation: Using the Routh formula, one can show that for

$$\alpha < \tfrac{1}{2}(-3.5 + \sqrt{(3.5)^2 + 280}) \approx 6.8.$$

P^+ and P^- are stable. At

$$\alpha = \tfrac{1}{2}(-3.5 + \sqrt{(3.5)^2 + 280})$$

a pair of eigenvalues crosses the imaginary axis and Hopf bifurcation occurs, thereby signifying the birth of a periodic orbit. Hopf bifurcation here, however, should be interpreted in its generalized sense, because the right-hand side of (2.4) is only continuous but not a C^4 function. Box ☐2 shows two distinct periodic attractors (stable limit cycles) at

$$\alpha = 8.0$$

projected onto the (z, x)-plane. Note that any asymmetric periodic attractor must occur in pair because (2.4) is symmetric with respect to the origin.

2) Period Doubling: As we increase α slightly beyond 8.0, a period-doubling bifurcation is initiated. Box ☐3 shows the period-2 attractors at

$$\alpha = 8.2.$$

A further increase of α gives rise to period-4 orbits.

3) Rössler's Spiral-Type Attractor: At

$$\alpha = 8.5$$

the attractor (Box ☐4) no longer appears to be periodic. It has the structure of a Rössler's spiral-type attractor [11]. As we continue tuning the bifurcation parameter α, we observe that the spiral-type attractor persists up to

$$\alpha < 8.5.$$

4) Periodic Window: At

$$\alpha \approx 8.575$$

a periodic window in Box ☐5 is observed. After this, a spiral-type attractor is observed again.

5) Rössler's Screw-Type Attractor: As we increase α further, the above spiral-type attractor eventually deforms into a Rössler's screw-type attractor [11].

6) The Double Scroll: As we increase α further, the attractor abruptly enlarges itself and creates two holes located symmetrically with respect to the origin, which corresponds to the parameter value

$$\alpha = 9.0.$$

This is the double-scroll attractor (see Box ☐6). This attractor appears to persist over the parameter interval

$$8.81 < \alpha < 10.05.$$
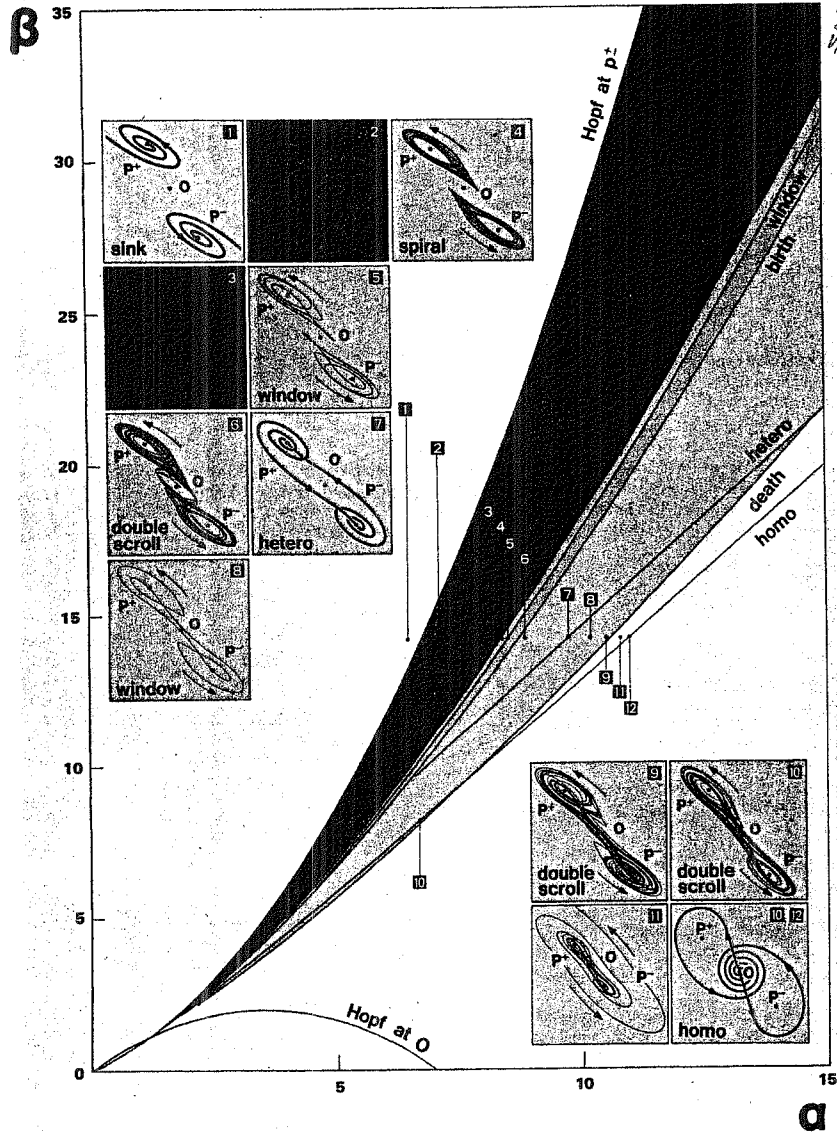
However, at the parameter value

$$\alpha = 10.05$$

Fig. 18. Two-parameter bifurcation diagram in the (α, β)-plane.

---

the periodic window in Box $\boxed{8}$ is observed. After this, several other strange-looking windows are seen.

7) Heteroclinicity: At

$$\alpha \approx 9.78$$

one observes that the two "holes" of the double scroll become extremely small. In fact, the trajectory almost hits $P^{\pm}$ and spends an extremely long period of time around $P^{\pm}$. This signifies the heteroclinic trajectory depicted in Box $\boxed{7}$. One can prove the existence of a horseshoe in a manner similar to the proof given in (2.4). The heteroclinicity of the double scroll is discussed in [6], [9], and [13].

8) Boundary Crisis: Box $\boxed{9}$ shows the attractor at

$$\alpha = 10.5.$$

Suddenly, however, at

$$\alpha \approx 10.75$$

the attractor disappears: (2.4) diverges with *any* initial condition (see Box $\boxed{11}$)! This disappearing act provokes the interesting question as to how the attractor dies. A careful analysis suggests that this phenomenon is related to the simultaneous presence of a *saddle-type* closed orbit encircling the attractor (the broken line curve in Fig. 5). With a slight increase in α beyond 10.5, the attractor appears to collide with the saddle-type periodic orbit. This collision provides a natural mechanism leading to the attractor's death. Note that if the attractor stays away from the *saddle-type* closed orbit, there would be no way for the trajectory in the attractor to escape. If, however, the attractor *collides with* the saddle-type closed orbit, then it would provide an exit path for the trajectory to escape into the outer space. This is what happens at $\alpha \approx 10.75$, which signifies a boundary crisis.

Box $\boxed{10}$ shows the attractor at the parameter value where the homoclinicity of (2.4) occurrs. Box $\boxed{10}\boxed{12}$ depicts the homoclinicity. Note that the symmetry of (2.4) implies that homoclinic trajectories are present in a pair. Finally, on the curve "Hopf at 0," the eigenspace $E^c(0)$ changes its stability type, while $E^r(0)$ is always unstable.

Looking at this bifurcation diagram, one sees that chaos can be *quenched* by making α sufficiently small, i.e., making C_1 sufficiently large, or making α sufficiently large, when β is fixed. In the former case, the trajectory converges to $P^{\pm}$, while in the latter case, the trajectory converges to the large periodic attractor [1], [9]. Similarly, chaos can be quenched by adjusting β appropriately when α is fixed.

In closing this section, there has been an interesting recent discovery of the fact that at certain parameter values the saddle-type periodic orbit is *stabilized* into a periodic attractor [14].

III. FOLDED TORUS

A. Circuitry

The circuit of Fig. 19(a) consists of only four elements among which only one is nonlinear: the piecewise-linear resistor characterized by Fig. 19(b). Linear elements L and C_2 are passive while the other capacitance has a negative value $-C_1$. The dynamics is given by

$$C_1 \frac{dv_{C_1}}{dt} = -g(v_{C_2} - v_{C_1})$$

$$C_2 \frac{dv_{C_2}}{dt} = -g(v_{C_2} - v_{C_1}) - i_L$$

$$L \frac{di_L}{dt} = v_{C_2} \tag{3.1}$$

where $v_{C_1}, v_{C_2},$ and i_L denote, respectively, the voltage across C_1, the voltage across C_2, and the current through L. The function $g(\cdot)$ denotes the v–i characteristic of the nonlinear resistor and is described by

$$g(v) = -m_0 v + 0.5(m_0 + m_1) [|v + E_1| - |v - E_1|]. \tag{3.2}$$

Fig. 20 gives a realization. Although the capacitance on the right-hand side is positive, the subcircuit N makes it act as a negative capacitance when looked at from the left-hand port of N.

B. Experimental Observations

We will give only two pictures at two different values of C_1. Fig. 21(a) shows a 2-torus, while Fig. 21(b) indicates a
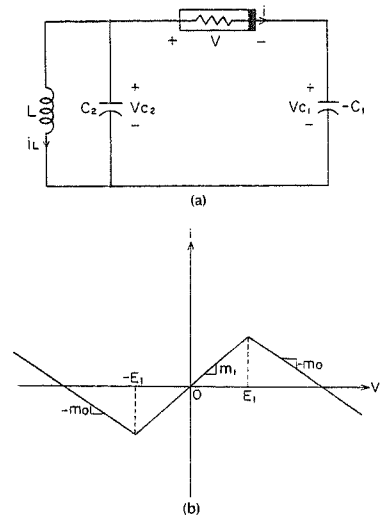

(a)

(b)

Fig. 19. A simple third-order autonomous circuit which exhibits a folded torus. (a) Circuitry. (b) Nonlinear resistor v–i characteristic.
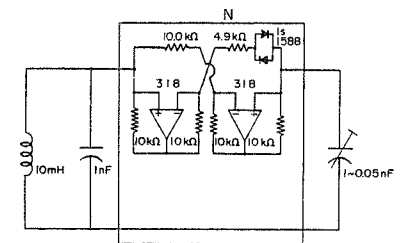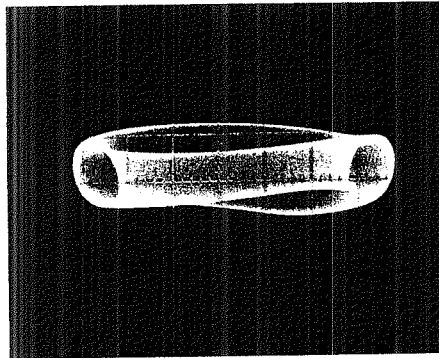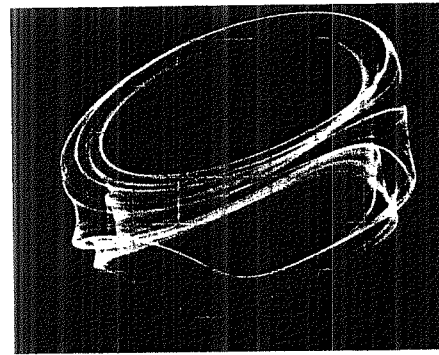

Fig. 20. Physical realization of the circuit in Fig. 19.

(a)

(b)

Fig. 21. Attractors observed from the circuit of Fig. 20 projected onto the (v_{C_1}, v_{C_2})-plane. Horizontal scale: 0.5 V/div. Vertical scale: 0.5 V/div. Only one of two attractors is shown. (a) 2-torus. (b) Folded torus.

"folded torus" [15]. In order to see them more clearly, let us look at Fig. 22 which shows the cross sections of the corresponding trajectories at $i_L = 0$, $v_{C_2} < 0$. It is clear that Fig. 21(a) is a 2-torus, while Fig. 21(b) looks like a folded torus.
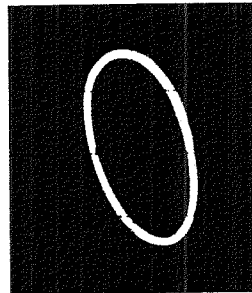
C. Confirmation

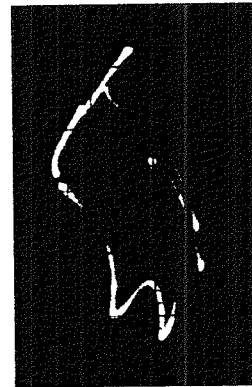Fig. 23 shows the corresponding simulation results.

D. Analysis

Let us transform (3.1) into the following dimensionless form:

$$\frac{dx}{dt} = -\alpha f(y - x)$$

$$\frac{dy}{dt} = -f(y - x) - z$$

$$\frac{dz}{dt} = \beta y \tag{3.3}$$

(a)

(b)

Fig. 22. Cross sections at $i_L = 0$, $v_{C_2} < 0$, of the corresponding trajectories from Fig. 20, on the (v_{C_1}, v_{C_2})-plane. (a) 2-torus. (b) Folded torus.

where

$$x = v_{C_1}/E_1 \qquad y = v_{C_2}/E_1 \qquad z = i_L/(C_2 E_1)$$

$$\alpha = C_2/C_1 \qquad \beta = 1/(LC_2) \qquad a = m_0/C_2$$

$$b = m_1/C_2 \tag{3.4}$$

$$f(x) = -ax + 0.5(a + b) \left[|x + 1| - |x - 1|\right]. \tag{3.5}$$

The rescaled parameters which correspond to the original circuit are

$$a = 0.07 \qquad b = 0.1 \qquad \beta = 1 \tag{3.6}$$

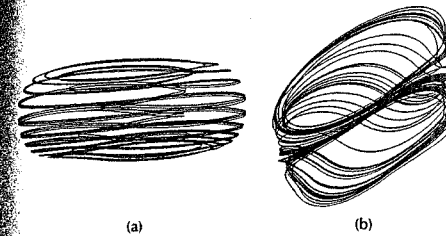and Fig. 23(a) (resp., Fig. 23(b)) corresponds to

$$\alpha = 2.0 \text{ (resp., } \alpha = 15.0).$$

Lyapunov exponents at $\alpha = 2.0$ (resp., $\alpha = 15.0$) are

$$\mu_1 \approx 0 \qquad \mu_2 \approx 0 \qquad \mu_3 \approx -0.00675 \tag{3.7}$$

$$\text{(resp., } \mu_1 \approx 0.027 \qquad \mu_2 \approx 0 \qquad \mu_3 \approx -0.1134). \tag{3.8}$$

Because no Lyapunov exponent in (3.7) is positive, the system is not chaotic. However, since only one Lyapunov expo-

(a)   (b)
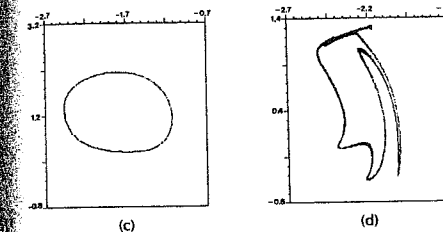
(c)   (d)

Fig. 23. Computer confirmation of Figs. 21 and 22. (a) Projection onto the (v_{C_1}, v_{C_2})-plane at $\alpha = 2.0$. (b) Projection onto the (v_{C_1}, v_{C_2})-plane at $\alpha = 15.0$. (c) Cross section at $i_L = 0$, $v_{C_2} < 0$, where $\alpha = 2.0$. (d) Cross section at $i_L = 0$, $v_{C_2} < 0$, where $\alpha = 15.0$.

nent is negative, the solution is not a periodic attractor, either. The presence of 2 zero Lyapunov exponents, therefore, provides a further confirmation that the trajectory in Fig. 21(a) is indeed a 2-torus, namely, a *quasi-periodic* solution. The largest Lyapunov exponent μ_1 in (3.8) is *positive*, which confirms that the trajectory in Fig. 21(b) is chaotic.

Let us look at typical trajectories in terms of the eigenspaces of equilibria as we did for the double scroll. First we partition the state space into three regions R_1, R_0, and R_{-1} separated by boundaries B_1 and B_{-1}, respectively, where (see Fig. 24)

$$R_1 = \{(x, y, z): y - x < -1\}$$

$$R_0 = \{(x, y, z): |y - x| < 1\}$$

$$R_{-1} = \{(x, y, z): y - x > 1\}$$

$$B_1 = \{(x, y, z): y - x = -1\}$$

$$B_{-1} = \{(x, y, z): y - x = 1\}.$$

System (3.3) has three equilibria, **0** and $P^{\pm}$. The eigenvalues at **0** (resp., $P^{\pm}$) consist of one real $\tilde{\gamma}_0$ (resp., $\tilde{\gamma}_1$) and a complex-conjugate pair $\tilde{\sigma}_0 \pm j\tilde{\omega}_0$ (resp., $\tilde{\sigma}_1 \pm j\tilde{\omega}_1$). In particular at $\alpha = 2$, $\beta = 1$

$$\tilde{\gamma}_0 \approx 0.14786 \qquad \tilde{\sigma}_0 \approx -0.048886 \qquad \tilde{\omega}_0 \approx 1.0060$$

$$\tilde{\gamma}_1 \approx -0.10425 \qquad \tilde{\sigma}_1 \approx 0.034426 \qquad \tilde{\omega}_1 \approx 1.0030. \tag{3.9}$$

Let $E^s(\mathbf{0})$ (resp., $E^u(\mathbf{0})$) denote the eigenspace corresponding to $\tilde{\gamma}_0$ (resp., $\tilde{\sigma}_0 \pm j\tilde{\omega}_0$). Similarly, let $E^u(P^{\pm})$ (resp., $E^s(P^{\pm})$) denote the eigenspace corresponding to $\tilde{\sigma}_1 \pm j\tilde{\omega}_1$ (resp., $\tilde{\gamma}_1$). While the patterns of the eigenvalues in (3.9) are identical to those of the double scroll, there are two subtle differences:

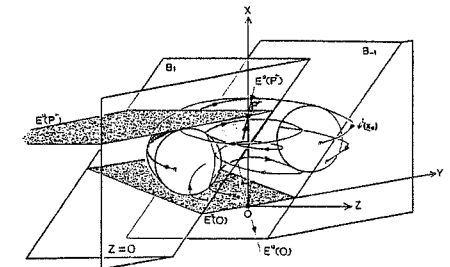i) The magnitude of $|\tilde{\gamma}_1|$ is not as large as in the double

Fig. 24. Typical trajectories.

scroll, hence the "flattening" of the attractor onto $E^u(P^{\pm})$ is relatively weak.

ii) $E^s(\mathbf{0})$ and $E^u(P^{\pm})$ are almost parallel with each other.

Let φ^t be the flow generated by (3.3) and pick an initial condition x_0 near **0** above $E^s(\mathbf{0})$ but not on $E^u(\mathbf{0})$. Since $\tilde{\gamma}_0 > 0$, $\varphi^t(x_0)$ starts moving up (with respect to the x-axis) while rotating clockwise around $E^u(\mathbf{0})$ (Fig. 24). Since (3.3) is linear in R_0, $\varphi^t(x_0)$ eventually hits B_1 and enters R_1. Because of the relative position of $E^s(P^{\pm})$, $\varphi^t(x_0)$ further moves up while this time rotating around $E^s(P^{+})$. Since $\tilde{\sigma}_1 > 0$, the solution $\varphi^t(x_0)$ *increases* its magnitude of oscillation and eventually enters R_0. Then, because of the relative positions of R_0 and R_1, $\varphi^t(x_0)$ starts moving downward (with rotation), eventually hits B_{-1}, and then flattens itself against $E^s(\mathbf{0})$ while rotating around $E^u(\mathbf{0})$. Since $\tilde{\sigma}_0 < 0$, the solution *decreases* its magnitude of oscillation and gets into the original neighborhood of **0**. This process then repeats itself, *ad infinitum*, but never returning to the original point. Hence the associated loci densely cover the surface of a two-torus.

E. Bifurcations

Bifurcations of (3.3) are extremely rich. They even include the double scroll. Note that (3.3) and (3.5) have four parameters. We will fix a and b as in (3.6) and vary α and β. The appearance of a 2-torus indicates that one can look at the bifurcations in terms of **rotation numbers**. The rotation number ρ is defined for a homeomorphism h on a circle, namely

$$h: S^1 \rightarrow S^1$$

$$\rho = \lim_{n \to \infty} \frac{h^n(x) - x}{n}, \qquad x \in S^1.$$

(The limit always exists.) If ρ is *rational*, i.e., $\rho = m/n$, where m and n are positive integers, then the trajectory is n-periodic. In this case, all trajectories approach a unique n-periodic orbit, while winding around S^1 "m" times before completing one periodic orbit. Such behavior is called an $m:n$ **phase locking**. If ρ is *irrational*, then the orbit is **quasi-periodic** and, therefore, densely covers S^1.

In order to study the rotation number for (3.3), one has to find a subset homeomorphic to S^1 and that a homeomorphism h is indeed induced via the flow of (3.3) on it. Since this is an extremely difficult, if not impossible task, we *assume* that the rotation number can be defined in the following region:

$$\{(\alpha, \beta) | 1 < \alpha < b(\alpha)\}$$

where $b(\alpha)$ is a function which describes the curve B of Fig. 25, the bifurcation diagram. Let us explain Fig. 25 in more detail. On the line *DIV* which is the line $\alpha = 1$, the divergence of (3.3) is zero. For $0 < \alpha < 1$, a periodic attractor is observed, while for $\alpha > 1$, an attracting torus is observed (Fig. 22(a)).

The solid lines indicate the boundaries of the regions where the rotation numbers are constant, where 1:5 means that the rotation number $\rho = \frac{1}{5}$, etc. The chain lines denote curves on which period-doubling bifurcations occur. In order to avoid further complication of the picture, only the onset of the period-doubling cascade is shown. The broken lines indicate boundaries where chaos is observed. The symbol C stands for (folded torus) chaos whereas DS stands for the double scroll. These curves are obtained by observing the trajectories via Runge–Kutta iterations. Note that there are many regions in Fig. 25 where the rotation number is equal to some rational number. Such regions are called **Arnold tongues.**

A careful examination of Fig. 25 reveals the following empirical laws (for fixed β):

   i) If $\alpha_1 > \alpha_2$ and if $\rho(\alpha_1) = m_1/n_1$, $\rho(\alpha_2) = m_2/n_2$, then
$$\rho(\alpha_1) < \rho(\alpha_2).$$

   ii) There is an α_3 such that $\alpha_1 > \alpha_3 > \alpha_2$, $\rho(\alpha_3) = (m_1 + m_2)/(n_1 + n_2)$, and
$$\rho(\alpha_1) > \rho(\alpha_3) > \rho(\alpha_2).$$

Fig. 26 gives the graph of ρ as a function of α with $\beta = 1$. The resulting monotone-increasing function is called a **devil's staircase.** The graph is obtained by observing the trajectories via Runge–Kutta iterations.

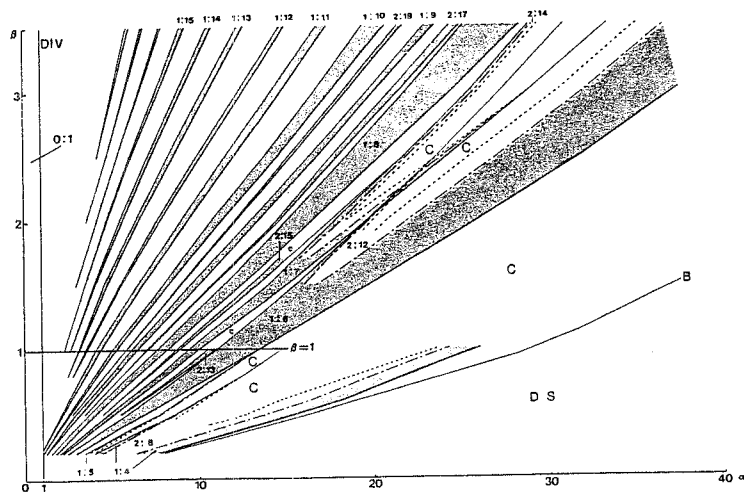In order to get a feeling of what is happening, let us fix β:
$$\beta = 1$$

and vary α:
$$0 < \alpha < 14.3.$$

Fig. 27 shows the bifurcation diagram of v_{C_1} on the cross section $i_L = 0$, $v_{C_2} < 0$. Let us explain this in terms of Fig. 25.

   i) As one moves along $\beta = 1$ in the 1:5 Arnold tongue, one hits the boundary of the 2:10 Arnold tongue, thereby signifying a period-doubling bifurcation.

   ii) When one moves to the right in the 1:6 Arnold tongue on the line $\beta = 1$, one does not hit the boundary of the 2:12 Arnold tongue. This explains why one does not observe any period-doubling cascade for the period-6 attractor.

   iii) As one moves to the right along the line $\beta = 1$, the circle map nature is destroyed before the system gets into the 1:6 phase-locking. This is why one observes a sudden bifurcation of 1:6 phase-locking into chaos. It appears that this chaotic attractor is born via an **intermittency** route. After 1:6 phase-locking, i.e., after all fixed points disappear via a *tangent bifurcation*, there are six regions called "channels." Inside each channel, a solution behaves like a periodic orbit because it spends a very long period of time in the channel. Once it gets out of the channel, however, the solution behaves in an erratic manner. Finally, we remark that the 1:5 Arnold tongue overlaps with the 1:4 Arnold tongue, hence the right-hand boundary of the 1:5 Arnold tongue cannot be observed clearly.

It should be noted that the above bifurcation scenario indicates a "torus breakdown" in the **third-order autonomous** circuit. Previous systems in which torus breakdowns have been observed are either nonautonomous [16], [17] or higher order [18], [19]. Also, previous work on torus breakdowns has been, to the best of our knowledge, either through laboratory measurement only [16] or by simulation
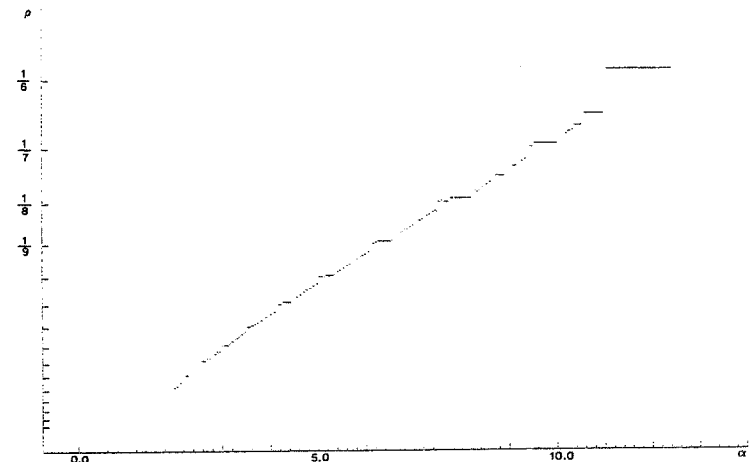
Fig. 26. The graph of ρ as a function of α at $\beta = 1$.
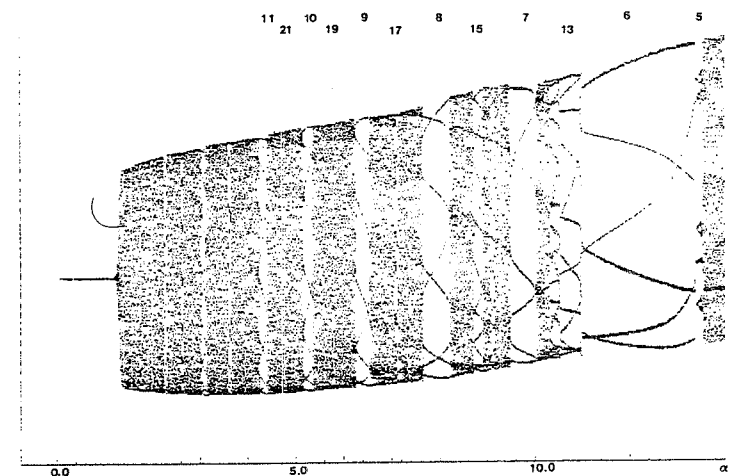
Fig. 27. One-parameter bifurcation diagram of v_{C_1} at $i_L = 0$, $v_{C_2} < 0$, where $\beta = 1$.

only [17]–[19]. Many more details of this section are found in [20].

IV. DRIVEN R-L-DIODE CIRCUIT

Both of the circuits discussed so far are *autonomous*, while the circuit in this section is *nonautonomous*, i.e., it is driven by an external voltage source.

A. Circuitry

Consider the R-L-Diode circuit of Fig. 28 driven by a sinusoidal voltage source where

$R = 107\ \Omega$ $L = 2.5$ mH

$f = \omega/2\pi = 150$ kHz $E = 6.2$ V

Diode: 3CC13.

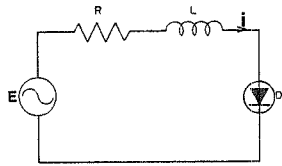**Fig. 25.** Two-parameter bifurcation diagram in the (α, β)-plane.

Fig. 28. Driven R–L-Diode circuit. $R = 107\ \Omega$, $L = 2.5\ mH$, $f = 150\ kHz$, Diode: 3CC13.

B. Experimental Observations

Fig. 29 shows the two-dimensional Poincaré section taken at each period $T = 1/f$ in the (voltage, current)-plane of the diode.
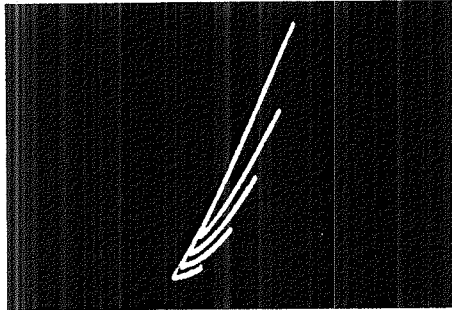

Fig. 29. Two-dimensional Poincaré section in the (voltage, current)-plane of the diode at $E = 6.2\ V$.

C. Confirmation

Although the circuit in Fig. 28 contains only three elements, its dynamics is rather involved in view of the non-linearities of the p-n junction diode, which are not purely resistive at frequencies above 100 kHz. A reasonably accurate circuit model of the diode [21] is given by Fig. 30, where both the resistor and the capacitor (Fig. 30(b)) are nonlinear. From extensive laboratory measurements and digital computer simulations, it has been observed [22] that in order to reproduce the same qualitative behavior, the nonlinear resistor in the above model is not essential. Moreover, the nonlinear q–v characteristic of the capacitor can be replaced by the drastically simpler two-segment piecewise-linear curve shown in Fig. 30(c), without changing the bifurcation pictures.

Fig. 31 shows the simulation corresponding to Fig. 29. The cross section, however, is taken on the (charge, current)-plane instead of the (voltage, current)-plane, due to a lack of time to prepare the material.

D. Analysis

To analyze the circuit, we will further simplify the dynamics, and then observe several key properties of the Poincaré
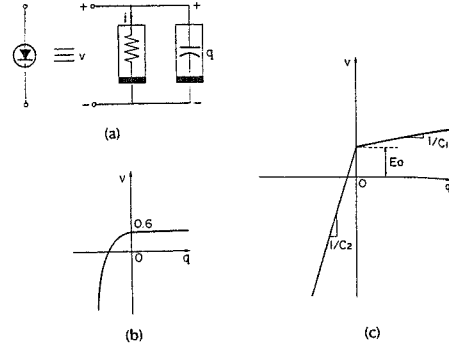

Fig. 30. Circuit model of a diode. (a) Original model (parallel connection of a nonlinear resistor and a nonlinear capacitor). (b) Characteristic of the nonlinear capacitor. (c) A drastically simplified capacitor characteristic without destruction of the essential features.

return map. Based upon these observations, we will propose a surprisingly simple two-dimensional map model which essentially captures the bifurcation pictures of the original circuit.

1) Further Simplification: In order to understand how a chaotic attractor is formed, we will further simplify the circuit of Fig. 28 with Fig. 30(c). Namely, we have observed that the sinusoidal voltage source can be replaced by a square-wave voltage source of the source period $T = 1/f$ without altering the essential features. Therefore, we will analyze the circuit shown in Fig. 32 where the nonlinear capacitor is characterized by Fig. 30(c). The dynamics of this circuit is described by

$$\frac{dQ}{d\tau} = I$$

$$L\frac{dI}{d\tau} = -RI - \begin{cases} \dfrac{1}{C_1}Q, & \text{if } Q \geq 0 \\ \dfrac{1}{C_2}Q, & \text{if } Q < 0 \end{cases}$$

$$- E_0 + \begin{cases} +E, & \text{if } nT \leq \tau < \left(n+\dfrac{1}{2}\right)T \\ -E, & \text{if } \left(n+\dfrac{1}{2}\right)T \leq \tau < (n+1)T \end{cases}$$

(4.1)

where we use Q, I, and τ to denote the original circuit variables. Defining the following normalized variables:

$$q = \frac{Lf^2}{E}Q \qquad i = \frac{Lf}{E}I \qquad t = f\tau$$

$$k = \frac{R}{Lf} \qquad \alpha = \frac{1}{LC_1f^2} \qquad \beta = \frac{1}{LC_2f^2}. \qquad (4.2)$$

Fig. 31. Confirmation. The cross section is taken on the (charge, current)-plane instead of the (voltage, current)-plane.
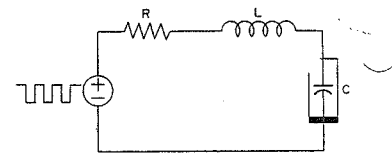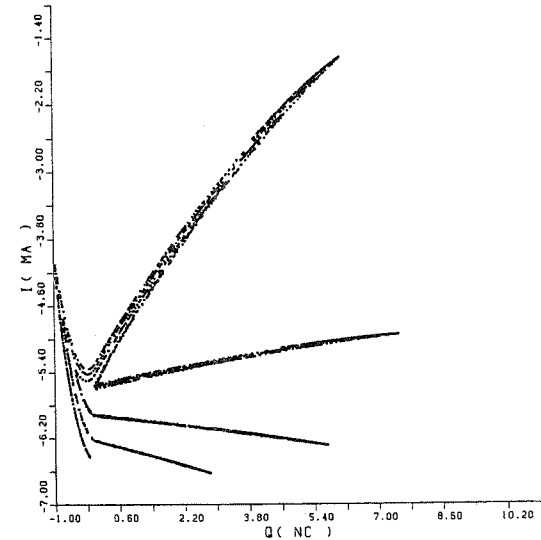

Fig. 32. Simplified circuit which captures essentially all the experimentally observed phenomena.

Equation (4.1) can be transformed into

$$\frac{dq}{dt} = i$$

$$\frac{di}{dt} = -ki - \begin{cases} \alpha q, & \text{if } q \geq 0 \\ \beta q, & \text{if } q < 0 \end{cases}$$

$$- \frac{E_0}{E} + \begin{cases} +1, & \text{if } n \leq t < \left(n+\dfrac{1}{2}\right) \\ -1, & \text{if } \left(n+\dfrac{1}{2}\right) \leq t < (n+1) \end{cases}$$

(4.3)

First observe that any solution of (4.3) is made up of components from the following four linear autonomous flows on $\mathbb{R}^2$

φ_1^t: $q \geq 0$ and the driving source is $V_s(t) = +1$

φ_2^t: $q < 0$ and the driving source is $V_s(t) = +1$

φ_3^t: $q \geq 0$ and the driving source is $V_s(t) = -1$

φ_4^t: $q < 0$ and the driving source is $V_s(t) = -1$.

Using the above simplified circuit model and solution components, we can uncover the essential features of the circuit dynamics with the help of the following observations:

i) The area contraction rate is constant and is strictly less than 1. This stems from the fact that the area contraction rate is determined by the divergence of (4.3), namely

area contraction rate = exp (divergence)
where divergence = $-k = -R/Lf$. (4.4)

ii) $0 \leq t < 1/2$.

Fig. 33 shows the flows φ_1^t and φ_3^t with $\alpha = 0.1$, $\beta = 10.0$. Each trajectory corresponds to a different initial condition.
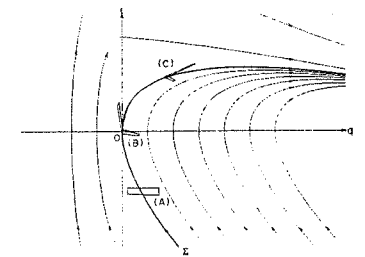

Fig. 33. Deformation of the initial rectangle A along a trajectory for $0 \leq t \leq 1/2$.

Consider the trajectory Σ, which passes through the origin. Pick a "thin" rectangle A at $t = 0$ as shown in the figure and look at how A is deformed along the flow φ_1^t as t increases. If the initial condition $(q_0, i_0) \in A$ lies to the right-hand side of Σ, then $\varphi_1^t(q_0, i_0)$ never hits the i-axis. On the other hand, if (q_0, i_0) lies on the left-hand side of Σ, then $\varphi_1^t(q_0, i_0)$ eventually hits the i-axis at some time $t_1 > 0$; namely, $(q_1, i_1) = \varphi_1^{t_1}(q_0, i_0)$. For $t > t_1$ the dynamics obeys the flow φ_2^t where eventually it again hits the i-axis at some time $t_2 > t_1$; namely, $(q_2, i_2) = \varphi_2^{t_2}(q_1, i_1)$, whereupon it reverts back to the original flow φ_1^t for $t > t_2$. The *key* observation here is that $\alpha < \beta$ implies that the vertical velocity (i.e., the i-axis) component of trajectories corresponding to φ_2^t is larger than that for φ_1^t. This implies that **the part of A which is on the left-hand side of Σ is stretched (in the vertical direction) more than the part on the right-hand side of Σ.** Note also that on the left-hand side of Σ, $q_1' < q_1$ implies that $\varphi_2^t(q_1', i_1)$ has a larger vertical stretching than $\varphi_2^t(q_1, i_1)$. These observations show that A is eventually deformed into sets B and C shown in Fig. 33.

iii) $1/2 \le t < 1$.

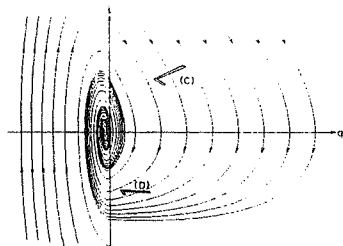After $t = 1/2$, the dynamics consists of component flows given by Fig. 34. Extensive computer simulations show that

Fig. 34. Deformation of the set C along a trajectory for $1/2 \le t \le 1$.

for $1/2 \le t < 1$, the set $\varphi_3^t(C)$ never hits the i-axis if the initial rectangle A in Fig. 33 is chosen appropriately.

Combining the above three observations, we see that during the period $0 \le t < 1$, rectangle A stretches, folds, and eventually returns to the original region D. Extensive numerical observations show that we can choose appropriate A and D such that $A \supset D$. During this transformation process, the area of A is continually being contracted. If this mechanism is repeated many times, it can give rise to a very complicated behavior, such as chaos. Fig. 35 gives a global picture of this transformation over one period of the flow φ^t.

2) Two-Dimensional Map Model: Based upon the preceding observations, we propose a surprisingly simple *two-dimensional map model* which mimics the transformation described in Fig. 35. Fig. 36 gives a more precise description of the transformation mechanism. A simple two-dimensional map which transforms the square $STUV$ in Fig. 36(a) into the lambda shaped set in Fig. 36(d) is described by

$$x_{n+1} = y_n - 1 + \begin{cases} a_1 x_n, & \text{if } x_n \ge 0 \\ -a_2 x_n, & \text{if } x_n < 0 \end{cases}$$

$$y_{n+1} = b x_n. \tag{4.5}$$

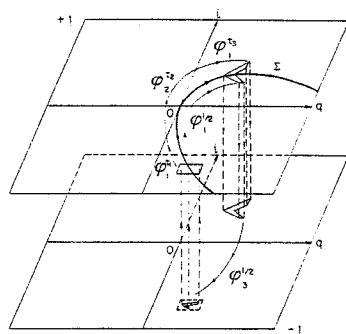**Fig. 35.** Overall picture of how the initial rectangle A is deformed and eventually returns to the initial region.
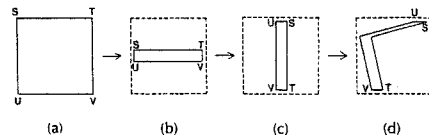

(a) (b) (c) (d)

Fig. 36. Two-dimensional map model. (a) The initial rectangle $STUV$. (b) The initial rectangle is compressed in the vertical direction. (c) The compressed rectangle is rotated by 90°. (d) The rectangle is bent into a lambda shape.

This map captures all the essential features of the bifurcations observed from the original circuit as shown in the following subsection.

E. Bifurcations

Fig. 37 gives an experimental observation showing the one-dimensional bifurcation diagram of the current i of the circuit of Fig. 28 when the amplitude E of the applied sinusoidal voltage source is increased periodically from 0 to 7.7 V (E is modulated by a sawtooth waveform). Each point in this "bifurcation tree" represents a *one-dimensional Poincaré section* taken at each fundamental period $T = 1/f$ of the sinusoidal source. There are two striking features in this bifurcation tree:

i) A succession of large periodic windows the periods of which *increase exactly by one* as we move from any window to the next window to the right.

ii) A succession of chaotic bands sandwiched between the large periodic windows.

The cross section in Fig. 29 corresponds to $E = 6.2$ V, i.e., the five chaotic bands of Fig. 37 correspond to the five "legs" of Fig. 29.

Let us examine how the simple map (4.5) captures the essential features of the bifurcation phenomena observed experimentally from the R–L-Diode circuit. Fig. 38 shows the one-parameter bifurcation diagram of x for (4.5) where

$$a_1 = 0.7 \quad b = -0.13$$

and a_2 is varied over the range
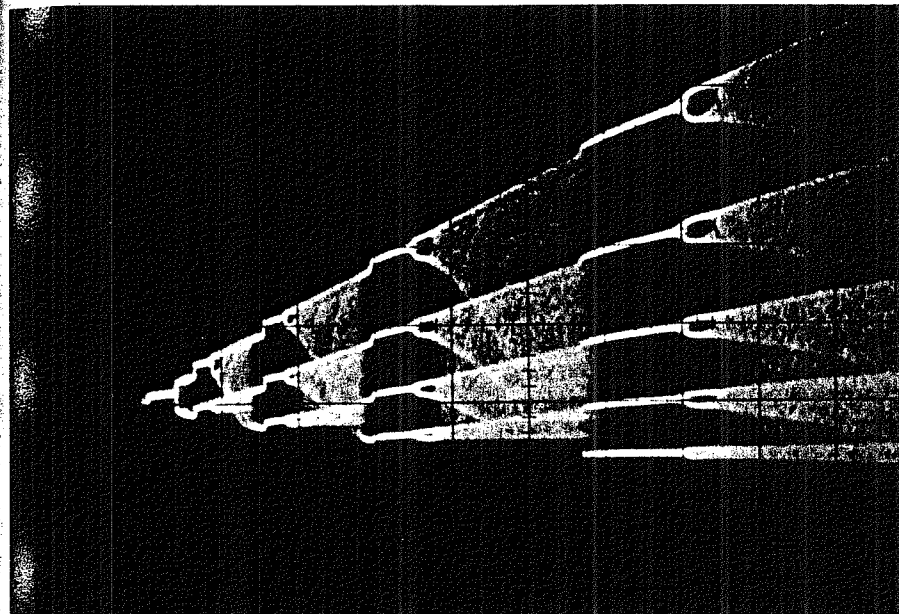
$$0 \le a_2 \le 20.$$

Fig. 37. One-dimensional bifurcation diagram of current i when amlitude E is increased from 0 to 7.7 V.
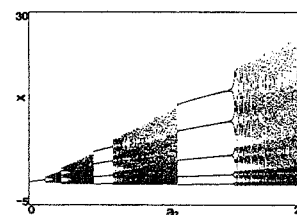

Fig. 38. One-parameter bifurcation diagram of x for the two-dimensional map model where $0 \le a_2 \le 20$.
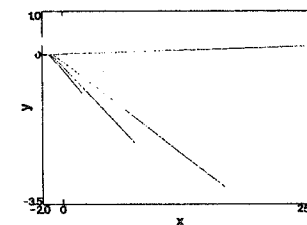

Fig. 39. Attractor observed from the two-dimensional map model at $a_2 = 18.0$.

Fig. 39 shows the attractor in the (x, y)-plane corresponding to

$$a_2 = 18.0.$$

Note that the attractor is *qualitatively* identical to the one obtained experimentally in Fig. 29.

A detailed analysis of (4.5) can be performed because of its simplicity. Based upon the bifurcation analysis of (4.5) one can understand the bifurcations of the original circuit. Fig. 40 shows the detailed bifurcation mechanism associated with the *period-4 window*. Bifurcations associated with other periodic windows have similar structures. The sequence of drawings in column B of Fig. 40 shows how the attractor of the two-dimensional map model is deformed as a_2 is increased from its value at the lowest position to a

larger value at the top position. The "snapshots" in column A show the corresponding experimental observations taken from the original R–L-Diode circuit as E increases from the bottom. The four insets in column C are enlarged pictures in a small neighborhood of the periodic point $P4A$ (of the two-dimensional map) identified by the solid triangles ▲.

We can now give a complete picture of what is happening in the original circuit.

i) Let us begin with the picture at the bottom in column B and look at the folded object. The symbol ☆ identifies the location of the *fixed-point Q* of (4.5) which is a *saddle* point for the present parameter range. As we increase the value of a_2 (E in the original circuit), a saddle-node bifurcation of *period-4* takes place *outside* the region where the attractor lives. This period-4 orbit has a strong influence on the
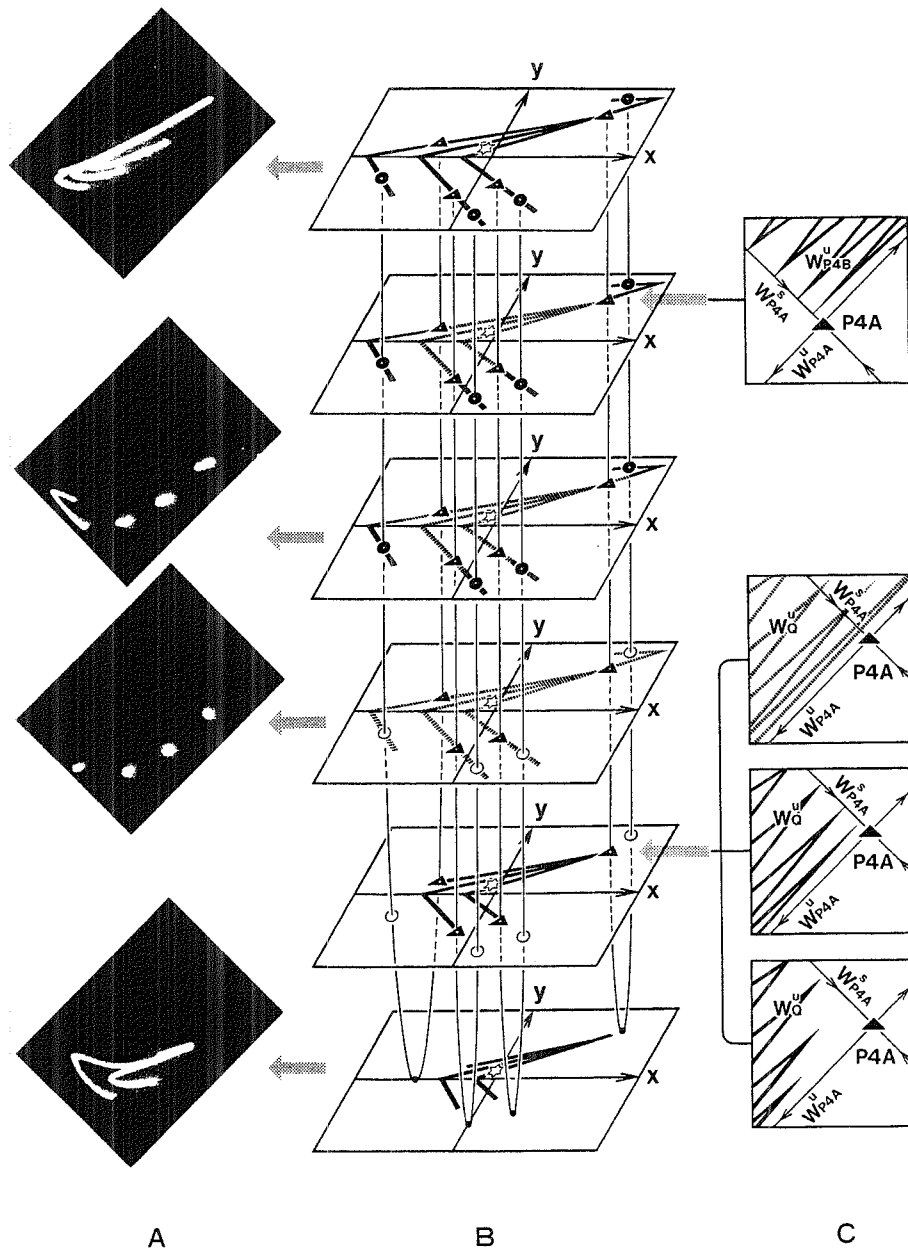
Fig. 40. Detailed bifurcation mechanisms corresponding to the period-4 window. Column A gives experimentally measured pictures, while the insets in column C show blown up pictures around P4A.

A   B   C

"structure" of the attractor. Since the bifurcation in this case corresponds to that of a saddle-node, a stable and unstable periodic orbits are born *in pairs* of one each.

ii) As we increase a_2 further, the unstable periodic orbit moves closer and closer to the attractor, and finally it *collides* with the attractor. This is depicted in the next to the last picture in column B, where the solid triangles ▲ (resp., open dots ○) correspond to an unstable (resp., stable) periodic orbit. The three insets in column C show the situation around the right-most unstable periodic point denoted by P4A.[5] The bottom inset (in column C) shows the situation before collision, where thick lines indicate W_Q^u, the unstable manifold of Q (the closure of which is conjectured to be the attractor).[6] As one increases a_2 by an appropriate amount, one sees that

$$\boxed{W_Q^u \text{ collides with } W_{P4A}^s} \qquad (4.6)$$

where W_{P4A}^s denotes the stable manifold of P4A. This is shown in the second inset from the bottom in column C, where W_Q^u is denoted by thick lines. A slight increase of a_2 leads to the situation depicted by the third inset from the bottom in column C, where, this time, W_Q^u is indicated by thick broken lines. The crucial observation in this picture is that the unstable direction of P4A **provides an orbit with an exit gate to escape** into the outer region. Because the stable and the unstable manifolds are *invariant*, a collision of the attractor with P4A is equivalent to a collision of the attractor with W_{P4A}^s.

iii) As there is now an exit gate, the attractor can no longer survive. Consequently, we observe the **sudden** disappearance or extinction of the attractor at the critical parameter value given by (4.6). This phenomenon, therefore, represents a **crisis**. After escaping into the outer region, however, the orbit *cannot diverge to infinity* because the *stable periodic orbit is waiting to attract it*. This situation is depicted in the third picture from the bottom in column B. This is the mechanism responsible for the extinction (death) of the "two-legged" attractor and the simultaneous emergence (birth) of a stable period-4 orbit.

iv) As we increase a_2 further, the stable period-4 orbit loses its stability via a *period-doubling* bifurcation. The limiting periodic attractor then changes into a *chaotic attractor* made up of four islets as depicted in the fourth picture from the bottom in column B. The *destablized* periodic points are denoted by four solid dots ●. Observe that the chaotic attractor in this case is the closure of the unstable manifold of ● rather than that of ☆ (see i)). Note also that the unstable period-4 points represented by the 4 solid triangles ▲ born in the preceding picture are still present near the chaotic attractor.

v) As we increase a_2 even further, the chaotic attractor eventually collides with the stable manifold of ▲; namely,

---
[5] Since this is a saddle-node bifurcation, a stable period-4 orbit and an unstable period-4 orbit are born simultaneously. One of the stable periodic points is denoted by P4B, whereas one of the unstable periodic points is called P4A.

[6] Generally it is conjectured [4] that a chaotic attractor is the closure of the unstable manifold of a periodic point. In fact, Misiurewicz [23] proved this fact rigorously for a piecewise-linear two-dimensional map (the Lozi map) which is similar to (4.5). Extensive simulations suggest that this appears to be the case for (4.5) as well.

$$\boxed{W_{P4B}^u \text{ collides with } W_{P4A}^s.} \qquad (4.7)$$

This is depicted in the third picture from the bottom in column B. The corresponding inset in column C shows the blown-up details around P4A. When (4.7) occurs, W_{P4B}^u plays the role of "bridging" between the chaotic islands, thereby giving birth to the attractor with "*three legs*" shown in the topmost picture in column B. Note that the increase in the number of legs (or the number of islands in the chaotic bands) is attributed to the interaction of the attractor with the other period-4 orbit which was born earlier via a saddle-node bifurcation.

Details of this section are found in [24], [25].

V. REMARKS

There is another interesting circuit [26] which cannot be included in this article due to the space limitation. The circuit exhibits a **hyperchaos** [27], i.e., it exhibits a chaotic attractor with *more than one positive* Lyapunov exponents. In other words, the dynamics expands not only small line segments but also small *area elements*, thereby giving rise to a "thick" attractor. This circuit appears to be the first real physical system where a hyperchaos has been observed experimentally *and* confirmed by computer. The reader is referred to [26].

The circuits described in this article are so simple that there must have been electrical engineers who "saw" chaos on their oscilloscopes and yet did not "recognize" it for what it was.[7] One cannot recognize a fact without having the corresponding *concept*.

The reader who has read this paper as well as other papers in this special issue, would understand (1.3) and (1.4) as well as (1.1) and (1.2), while in the past, only very few people (Poincaré, Birkoff, Einstein, and several others) were aware of them.

Finally, there is a famous story by Chuang Tsu (369-286 B.C.) (Fig. 41):

> The emperor of the South Sea was called Shu [Brief], the emperor of the North Sea was called Hu [Sudden], and the emperor of the central region was called **Hun-tun** [**Chaos**]. Shu and Hu from time to time came together for a meeting in the territory of Hun-tun, and Hun-tun treated them very generously. Shu and Hu discussed how they could repay his kindness. "All men," they said, "have seven openings so they can see, hear, eat, and breathe. But Hun-tun alone doesn't have any. Let's trying boring him some!"
> Every day they bored another hole, and on the seventh day Hun-tun died.
> (Translated by B. Watson [30])

Certainly, what scientists and engineers as well as other people have been doing in the past decade is to

> "bore holes in chaos."

---
[7] Van der Pol and Van der Mark say in their 1927 paper [28] "Often an irregular noise is heard in the telephone receivers before the frequency jumps to the next lower value. However, this is a subsidiary phenomenon, the main effect being the regular frequency demultiplication."

Fig. 41. Chuang Tsu's story of chaos [29].

This, however, is the very thing they have been doing to everything *mysterious* all the time. When the mystery is eventually cleared up by analysis, characterization, proof, etc., it ceases to be a mystery; it is *objectified*. The word "death" should perhaps be understood in this sense.

REFERENCES

[1] T. Matsumoto, L. O. Chua, and M. Komuro, "The double scroll," *IEEE Trans. Circuits Syst.*, vol. CAS-32, pp. 797–818, Aug. 1985.
[2] T. Matsumoto, L. O. Chua, and K. Tokumasu, "Double scroll via a two-transistor circuit," *IEEE Trans. Circuits Syst.*, vol. CAS-33, pp. 828–835, Aug. 1986.
[3] L. P. Shilnikov, "A case of the existence of a denumerable set of periodic motions," *Dokl. Sov. Math.*, vol. 6, pp. 163–166, 1965.
[4] J. Guckenheimer and P. Holmes, *Nonlinear Oscillations, Dynamical Systems, and Bifurcations of Vector Fields*. New York, NY: Springer-Verlag, 1983.
[5] A. Arneodo, P. Coulett, and C. Tresser, "Oscillators with chaotic behavior: An illustration of a theorem by Shilnikov," *J. Stat. Phys.*, vol. 27, pp. 171–182, 1982.
[6] L. O. Chua, M. Komuro, and T. Matsumoto, "The double scroll family," *IEEE Trans. Circuits Syst.*, vol. CAS-33, no. 11, pp. 1073–1118, Nov. 1986.
[7] T. Matsumoto, L. O. Chua, and K. Ayaki, in preparation.
[8] P. Glendinning and C. Sparrow, "Local and global behavior near homoclinic orbits," *J. Stat. Phys.*, vol. 35, pp. 645–697, 1984.
[9] T. Matsumoto, L. O. Chua, and M. Komuro, "The double scroll bifurcations," *Int. J. Circuit Theory Appl.*, vol. 14, pp. 117–146, Apr. 1986.
[10] ——, "Birth and death of the double scroll," *Physica D*, in press.
[11] O. E. Rössler, "Continuous chaos—Four prototype equations," *Ann. N.Y. Acad. Sci.*, vol. 316, pp. 376–392, 1979.
[12] C. Grebogi, E. Ott, and J. Yorke, "Chaotic attractor in crisis," *Phys. Rev. Lett.*, vol. 48, pp. 1507–1510, 1982.
[13] A. I. Mees and P. B. Chapman, "Homoclinic and heteroclinic orbits in the double scroll attractor," to be published in *IEEE Trans. Circuits Syst.*, vol. CAS-34, no. 9, Sept. 1987.
[14] D. P. George, "Bifurcations in a piecewise linear system," *Phys. Lett. A*, vol. 118, no. 1, pp. 17–21, 1986.
[15] W. F. Langford, *Numerical Studies of Torus Bifurcations* (International Series of Numerical Mathematics, vol. 70) Heidelberg/New York: Springer-Verlag, pp. 285–295.
[16] J. Stavans, F. Heslot, and A. Libchaber, "Fixed winding number and the quasi-periodic route to chaos in a convective fluid," *Phys. Rev. Lett.*, vol. 55, no. 6, pp. 596–599, Aug. 5, 1985.
[17] T. Bohr, P. Bak, and M. Hogh Jensen, "Transition to chaos by interaction of resonances in dissipative system II. Josephson junctions, charge-density waves, and standard maps," *Phys. Rev. A*, vol. 30, no. 4, pp. 1960–1969, Oct. 1984.
[18] M. Sano and Y. Sawada, "Transition from quasi-periodicity to chaos in a system of coupled nonlinear oscillator," *Phys. Lett.*, vol. 97A, no. 3, pp. 73–76, Aug. 15, 1983.
[19] V. Franceschini, "Bifurcation of tori and phase locking in a dissipative system of differential equations," *Physica 6D*, pp. 285–304, 1983.
[20] T. Matsumoto, L. O. Chua, and R. Tokunaga, "Chaos via torus breakdown," *IEEE Trans. Circuits Syst.*, vol. CAS-34, pp. 240–253, Mar. 1987.
[21] *Electronics Designer's Handbook*, 2nd ed. New York, NY: McGraw-Hill, 1977.
[22] T. Matsumoto, L. O. Chua, and S. Tanaka, "Simplest chaotic nonautonomous circuit," *Phys. Rev. A*, vol. 30, pp. 1155–1158, 1984.
[23] M. Misiurewicz, "The Lozi mapping has a strange attractor," *Ann. N.Y. Acad. Sci.*, vol. 316, pp. 348–358, 1979.
[24] T. Matsumoto, L. O. Chua and S. Tanaka, "Bifurcations in a driven R–L Diode circuit," in *Proc. IEEE Int. Symp. on Circuits and Systems*, pp. 851–854, 1985.
[25] S. Tanaka, T. Matsumoto, and L. O. Chua, "Bifurcation scenario in a driven R–L Diode circuit," *Physica D*, in press.
[26] T. Matsumoto, L. O. Chua, and K. Kobayashi, "Hyperchaos: Laboratory experiment and numerical confirmation," *IEEE Trans. Circuits Syst.*, vol. CAS-33, no. 11, pp. 1143–1147, 1986.
[27] O. E. Rössler, "Chaotic oscillations—An example of hyperchaos," in *Nonlinear Oscillations in Biology* (Lectures in Applied Mathematics, vol. 17). New York, NY: Amer. Math. Soc., 1979, pp. 141–156.
[28] B. Van der Pol and J. Van der Mark, "Frequency demultiplication," *Nature*, vol. 120, no. 3019, pp. 363–364, 1927.
[29] 1525 Chinese Edition (printed during the Ch'ing Dynasty).
[30] B. Watson, *The Complete Works of Chuang Tsu*. New York, London: Columbia Univ. Press, 1968.

Takashi Matsumoto (Fellow, IEEE), for a photograph and biography, please see page 981 of this issue.